Synergistic interactions of thermodiffusive instabilities and turbulence in lean hydrogen flames

Synergistic Interactions of Thermodiffusive Instabilities and Turbulence in Lean Hydrogen Flames

Lukas Berger[a,*], Antonio Attili[b], Heinz Pitsch[a]

[a] *Institute for Combustion Technology, RWTH Aachen University, 52056 Aachen, Germany*
[b] *Institute for Multiscale Thermofluids, School of Engineering, University of Edinburgh, Edinburgh, EH9 3FD, United Kingdom*

Abstract

Interactions of thermodiffusive instabilities and turbulence have been investigated by large-scale Direct Numerical Simulations (DNS) in this work. Two DNS of turbulent premixed lean hydrogen/air flames have been performed in a slot burner configuration at the same jet Reynolds number of $Re = 11,000$ and Karlovitz number of $Ka \approx 15$ using a detailed chemical mechanism. Realistic transport models are employed in one case, which features the characteristic patterns of thermodiffusively unstable flames, such as strong variations of the heat release and super-adiabatic temperatures. In the other case, the diffusivities of all species are set equal to the thermal diffusivity (unity Lewis numbers assumption) and thermodiffusive instabilities are therefore suppressed.

The local burning of the turbulent flame without thermodiffusive instabilities is similar to an unstretched laminar flame and the turbulent flame speed increases only due to the increase of flame surface area in agreement with previous studies for flames at similar conditions. In contrast, the thermodiffusively unstable flame features a strong enhancement of the turbulent flame speed, which is not only caused by flame wrinkling, but is greatly increased due to significant variations of the local reaction rates. These are caused by variations of the local equivalence ratio due to the differential diffusion of hydrogen. A comparison with a thermodiffusively unstable laminar flame at the same conditions reveals that the variations of the local equivalence ratio and local reaction rates are significantly enhanced in the turbulent flame due to higher fluctuations of curvature and an enhanced average strain rate induced by turbulence. Thus, turbulence and thermodiffusive instabilities show synergistic effects, which are reflected in a significantly higher fuel consumption rate per flame surface area. The flame surface area generation, which is governed by the tangential strain and the flame propagation in curved flame segments, is also different in the two cases. Most noteworthy, the tangential strain rate is shown to be determined by the smallest turbulent structures in both turbulent flames and to be unaffected by the thermodiffusive instability mechanism. However, thermodiffusive instabilities lead to a production of flame surface area in convexly curved flame segments, featuring the formation of tongue-like structures that penetrate into the unburned gas, which do not exist in the turbulent flame with unity Lewis numbers. This is linked to an enhancement of the flame displacement speed with curvature in the thermodiffusively unstable flame, while in the absence of instabilities, a reduction of the flame displacement speed with increasing curvature is observed, leading to a destruction of flame surface area.

These findings suggest that thermodiffusive instabilities are sustained in turbulent flows and even show synergistic interactions with turbulence, which needs to be accounted for in turbulent combustion models.

Keywords: Thermodiffusive Instability, DNS, Hydrogen, Premixed, Preferential Diffusion

1. Introduction

The recent rise of renewable energy sources is promoting the use of hydrogen as a carbon-free energy carrier [1]. One possibility to harness the energy stored in hydrogen is its usage in thermochemical energy conversion processes such as in gas turbines, industrial burners, or piston engines [2]. However, a variety of problems arise for combustion processes that involve hydrogen as a fuel. Lean hydrogen/air flames are prone to intrinsic combustion instabilities and, in particular, thermodiffusive instabilities, which can substantially change flame dynamics, heat release rates, and flame speeds. These aspects are highly relevant for the safe operation of any combustion device, e.g., to avoid flame flashback, but can also increase thermal efficiencies [3].

Thermodiffusive instabilities originate from the large disparity of the mass and thermal diffusive fluxes, which induces strong differential diffusion effects along the flame front. The ratio of the mass and thermal diffusivity is the Lewis number, which is particularly low for hydrogen. The strong differential diffusion of hydrogen leads to an amplification of small flame front perturbations such that strongly wrinkled flame fronts are observed with a significantly enhanced flame speed and strong variations of the local reaction rates. For example, Berger et al. [4] showed that thermodiffusive instabilities can lead to four times higher flame speeds compared to the unstretched laminar burning velocity in laminar lean hydrogen/air mixtures at ambient conditions.

The characteristic features of thermodiffusively unstable

*Corresponding author
Email address: l.berger@itv.rwth-aachen.de (Lukas Berger)

flames, such as the formation of small cellular structures, the strong variability of reaction rates along the flame front, and the enhanced consumption speed, have been extensively studied in laminar flows [4–10]. In particular, the enhancement of the overall consumption speed is found to be not only caused by an increase of flame surface area, but also by an enhanced fuel consumption rate per flame surface area, which is referred to as the stretch factor I_0. Due to the differential diffusion of hydrogen, significantly enhanced reaction rates are observed in flame segments that are convexly curved towards the unburned gas and extinction pockets are seen in concavely curved flame segments leading to an overall enhancement of fuel consumption rates. The variation of the local reactivity and consumption speed with different conditions has been discussed by Berger et al. [11, 12], who reported a significant increase of the flame consumption speed and the stretch factor I_0 towards lean mixtures, low temperatures, and high pressures indicating an increasing impact of thermodiffusive instabilities on the flame reactivity for these conditions.

However, combustion in applications of industrial relevance is typically impacted by interactions with a turbulent flow, necessitating a comprehensive understanding of thermodiffusive instabilities in turbulent flows. While theoretical works [13–15] expect flame intrinsic instabilities to be particularly relevant for low Karlovitz numbers, the exact region of influence in the turbulent combustion regime diagram and the identification of all relevant parameters is yet unclear. Early numerical studies [16–19] have assessed turbulent hydrogen flames in two-dimensional configurations indicating that the existence of the characteristic features of thermodiffusively unstable flames, such as super-adiabatic temperatures and increased local burning rates, are also sustained in turbulent flows. To study turbulence-flame interactions in three-dimensional flows, Aspden et al. [20–23] investigated turbulent lean premixed hydrogen flames in homogeneous isotropic turbulence at different Karlovitz numbers using Direct Numerical Simulations (DNS). Similar to the two-dimensional studies, large cellular structures along with extinction events and super-adiabatic temperatures are visible at low Karlovitz numbers. At high Karlovitz numbers, the large cellular structures become increasingly disrupted and several smaller-scale structures with increased burning rates and thinner flame fronts are formed. Further, the variations of the local equivalence ratio within the flame front due to differential diffusion become significantly smaller towards high Karlovitz numbers as turbulent mixing increasingly dominates molecular diffusion. While these findings suggest that the effects of differential diffusion eventually disappear at sufficiently high Karlovitz number, thermodiffusive instabilities were found to be present for a large range of Karlovitz numbers. Significant super-adiabatic temperatures are still visible, for instance, at a Karlovitz number of $Ka = 100$ [22]. Further DNS of hydrogen/air flames have been performed [24, 25], but these simulations do not feature thermodiffusive instabilities as either stoichiometric conditions or sufficiently high unburned temperatures are chosen to suppress thermodiffusive instabilities. The existence of the effects of differential diffusion in turbulent flames was also observed experimentally by Wu et al. [26], who analyzed hydrogen/air flames at different equivalence ratios in a coaxial round jet at jet Reynolds numbers up to $Re = 40,000$, where the Reynolds number is defined by the pipe's diameter and the bulk velocity. They reported a higher distortion and higher turbulent burning velocity for the lean cases due to the effects of differential diffusion. Similarly, Ahmed et al. [27] experimentally showed that in spherically expanding hydrogen flames, the effects of thermodiffusive instabilities lead to a strong enhancement of the stretch factor, indicating an increase of the local flame propagation due to intrinsic instabilities. Recently, Rocco et al. [28] also investigated the effects of differential diffusion in a lean hydrogen flame with an equivalence ratio of $\phi = 0.5$ at ambient conditions in a round Bunsen burner configuration, which features realistic shear driven turbulence. They used a reduced five-step mechanism and set the jet Reynolds number to $Re = 3,000$ and a Karlovitz number close to unity. Similar to previous studies, they observed super-adiabatic temperatures and significant variations of the local reactivity and the local equivalence ratio in flame segments that are convexly or concavely curved towards the unburned. While two distinct states of locally richer and leaner mixtures are seen in the statistics, the average local equivalence ratio reveals less variations than in an unstretched flamelet, so they conclude that turbulence homogenizes the local state of the mixture towards the nominal equivalence ratio.

As the effects of differential diffusion are found to be sustained in turbulent flames for a large range of Reynolds and Karlovitz numbers, it is of particular interest to develop a detailed understanding of the interactions of turbulence and thermodiffusive instabilities. In particular, it is yet unclear whether their interactions possibly reveal synergistic effects beyond their individual contributions. For instance, both mechanisms affect the flame wrinkling and the local reactivity of the flame, which both affect the fuel consumption rates and, hence, the turbulent flame speed. Thus, it is critical to assess their individual contributions and possible interactions.

To pursue a detailed investigation of such interactions, DNS, which can provide instantaneous and highly resolved species, temperature, and turbulent flow fields, are performed in this work. The DNS feature lean hydrogen/air flames in a slot burner configuration under realistic conditions such as shear driven turbulence, at high jet Reynolds numbers, a detailed chemical reaction mechanism, and realistic transport models including for instance the Soret effect, which was shown to be important in hydrogen flames [29, 30]. To systematically assess the interactions of thermodiffusive instabilities and turbulence, two DNS at ambient conditions with the same equivalence ratio and at the same Reynolds number of $Re = 11,000$ and Karlovitz number of $Ka \approx 15$ were performed. While one case uses realistic transport models, identical thermal and species diffusivities are used in the other case to suppress thermodiffusive instabilities. In the following, the DNS configuration and numerical methods are described first, followed by an analysis of the two flames that investigates the impact of turbulence, thermodiffusive instabilities, and their interactions on the turbulent flame speed.

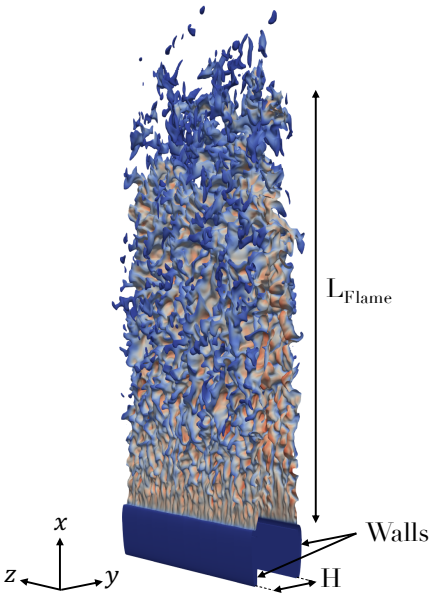

Figure 1: Visualization of the *TurbUnstable* flame represented by an iso-surface of temperature that is colored by the heat release.

Table 1: Simulation parameters and features of the two turbulent flames: Slot width H and bulk velocity U of central jet inflow, velocity U_{Coflow} of laminar coflow, laminar burning velocity s_{L} and thermal flame thickness l_{F} of an unstretched laminar flame, Kolmogorov length scale η evaluated on the mean flame sheet at half of the flame height, grid resolution Δ in x- and z-direction and for $|y| < 2.5H$ in y-direction, flame height L_{Flame}, jet Reynolds number Re, Karlovitz number Ka in the plateau region of Fig. 2, domain size L_{i}, and number of grid points N_{i} in each direction.

	TurbUnstable	TurbStable
H [mm]	8	4
U [m/s]	24	48
U_{Coflow} [m/s]	3.6	7.2
s_{L} [m/s]	0.17	0.34
l_{F} [μm]	714	374
η [μm]	180	90
Δ [μm]	70	35
L_{Flame}/H	8.5	26.3
Re	11,000	11,000
Ka	20	16
$[\frac{L_{\mathrm{x}}}{H}, \frac{L_{\mathrm{y}}}{H}, \frac{L_{\mathrm{z}}}{H}]$	[15, 12.5, 4.6]	[30, 20, 4.6]
$[N_{\mathrm{x}}, N_{\mathrm{y}}, N_{\mathrm{z}}]$	[1792, 1024, 512]	[3300, 1062, 512]

2. Configuration and Numerical Methods

2.1. Configuration

Large-scale DNS of a three-dimensional premixed lean hydrogen/air flame have been performed in a slot burner configuration surrounded by a coflow of burned gas. Simulations in the same type of configuration have been already performed, e.g. for methane/air flames by Sankaran et al. [31] and Luca et al. [32], and for stoichiometric hydrogen/air flames, which do not feature thermodiffusive instabilities, by MacArt et al. [25]. Fig. 1 shows a visualization of the slot burner configuration and the flame. The unburned mixture is set to an equivalence ratio of $\phi = 0.4$, an unburned temperature of $T_{\mathrm{u}} = 298$ K, and a pressure of $p = 1$ bar as significant thermodiffusive instabilities were observed for these conditions in laminar flames [4, 12]. The coflow consists of burned gas at the same conditions as the central jet with a temperature equal to the adiabatic temperature of $T_{\mathrm{b}} = 1418$ K. The mass fractions of all species for the central jet and coflow are provided in Tab. A2 in the supplementary material. Since thermodiffusive instabilities result from the significantly different diffusivity of the hydrogen molecule with respect to the other species, an additional DNS with diffusivities of all species equal to the thermal diffusivity and without the Soret effect was conducted as a reference case to suppress thermodiffusive instabilities and rigorously assess their effects (details on the different diffusivity models are provided further below). The two cases will be referred to as the *TurbUnstable* and *TurbStable* case, respectively.

An overview of the simulation parameters can be found in Tab. 1. The smaller computational domain for the *TurbUnstable* case results from a shorter flame due to a larger turbulent flame speed. As shown in Fig. 1 and similar to the configuration of Luca et al. [32], the central jet and the coflow streams are separated at the inlet by walls of thickness $H/20$, where H is the slot width. It is worth noting that the wall temperature is set to $T_{\mathrm{Wall}} = 298$K to avoid possible flashback events and for the velocities, a no-slip boundary condition is applied at the walls. The domain is periodic in the spanwise direction (z), open boundary conditions are prescribed at the outlet in streamwise direction (x), and slip conditions are imposed at the boundaries in crosswise direction (y). The inlet velocities of the central jet are taken from an auxiliary fully developed turbulent channel flow simulation and laminar coflows are applied outside of the central jet, featuring a uniform velocity, which corresponds to 15% of the bulk velocity U of the central jet, cf. Tab. 1.

Both DNS feature the same jet Reynolds number of $Re = 11,000$, which is defined as

$$Re = \frac{UH}{\nu_{\mathrm{u}}}, \tag{1}$$

where ν_{u} is the kinematic viscosity. The Karlovitz number is defined by the ratio of the flame and Kolmogorov time-scales, which can be written in terms of flame thickness l_{F} and Kolmogorov length scale η as

$$Ka = \left(\frac{l_F}{\eta}\right)^2, \tag{2}$$

where the flame thickness is defined by the maximum temperature gradient criterion in an unstretched laminar flame as

$$l_{\mathrm{F}} = \frac{T_{\mathrm{b}} - T_{\mathrm{u}}}{\max(|\nabla T|)}, \tag{3}$$

where T_{b} and T_{u} are the adiabatic and unburned temperature. The Kolmogorov length scale η is determined from the Favre-averaged energy dissipation rate $\widetilde{\epsilon}$ and the average kinematic

viscosity $\bar{\nu}$ as $\eta = (\bar{\nu}^3/\widetilde{\epsilon})^{1/4}$ [33]. Ensemble averages are performed in time and the statistically homogeneous z-direction. The value of η is taken at the position of the mean flame sheet, which is defined by the Favre-averaged progress variable field at $\widetilde{C}_{\mathrm{H_2}} = 0.8$ (the definition of the progress variable $C_{\mathrm{H_2}}$ is discussed later). To obtain the same Karlovitz number in both flames, the slot width H of the *TurbStable* case is halved compared to the *TurbUnstable* case as the flame thickness l_{F} of case *TurbStable* is approximately half of the flame thickness of case *TurbUnstable* due to the different diffusivity models in the two flames. Consequently, the bulk velocity of case *TurbStable* is doubled compared to case *TurbUnstable*, so the same Reynolds number is obtained. Fig. 2 shows the evolution of the local Karlovitz number Ka in the streamwise direction. For both flames, a Karlovitz number of $Ka \approx 15$ is obtained for large parts of the flame even though an increase of Karlovitz number towards the flame tip occurs in the *TurbUnstable* flame resulting from a flame-induced increase of the turbulent kinetic energy, similar to the observations of Chakraborty et al. [15]. The value of Ka in Tab. 1 is taken at half of the jet height for both flames.

The simulations of the two flames were initialzied by injecting the unburned gas of the central jet into a quiescent fluid, whose temperature and species mass fractions have been set to the conditions of the burned gas. To remove any effects from the initialization, the simulations were run sufficiently long and at least for one flow-through time based on the velocity of the coflow. Thereafter, statistics were collected for at least one flow through time based on the velocity of the central jet.

In addition to the two turbulent flames, a DNS of a three-dimensional laminar initially planar hydrogen/air flame at the same thermochemical conditions ($\phi = 0.4$, $T_{\mathrm{u}} = 298\mathrm{K}$, $p = 1\mathrm{bar}$) has been considered for comparison. This case, referred to as *LamUnstable* case, allows for the rigorous separation of the impact of the turbulent flow and the intrinsic flame instabilities on the flame evolution. Fig. 3 shows a snapshot of the laminar flame, where unburned mixture is entering the simulation domain at the lower boundary in y-direction, the burned gas leaves the simulation at the upper boundary in y-direction, and periodic boundary conditions are applied in the lateral x- and z-directions. The domain sizes are $L_{\mathrm{x}} = L_{\mathrm{z}} = 34 l_{\mathrm{F}}$ in the lateral directions and $L_{\mathrm{y}} = 95 l_{\mathrm{F}}$ in y-direction. While this domain confines the large-scale corrugations and is hence not large enough to feature a domain-independent value of the consumption speed [4], this DNS allows for an analysis of the local flame state and stretch factor, which are not affected by the domain size as they are determined by the small-scale wrinkling rather than the large-scale corrugations. In particular, the same simulation with a halved lateral domain size, $L_{\mathrm{x}} = L_{\mathrm{z}} = 17 l_{\mathrm{F}}$, has been performed, yielding different consumption seeds, but the same local flame state and stretch factor, which is shown in Figs. A1 and A2 in the supplementary material. The simulation is initialized by a harmonically perturbed flat flame and the constant velocity at the inlet is chosen such that the flame is stabilized sufficiently long in the simulation domain, a procedure which has been described in detail in Berger et al. [12]. In Fig. 3, strong variations of the heat release on the flame sheet are visible due to the thermodiffusive instability mechanism,

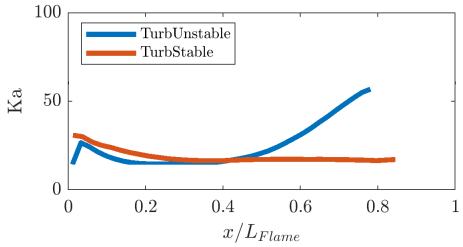

Figure 2: Variation of the local Karlovitz number Ka in the streamwise direction for the *TurbUnstable* and *TurbStable* case. Ka is evaluated on the mean flame sheet, which is defined by the Favre-averaged progress variable field at $\widetilde{C}_{\mathrm{H_2}} = 0.8$. L_{Flame} represents the flame height, which is defined when 99% of the average fuel mass flux is consumed.

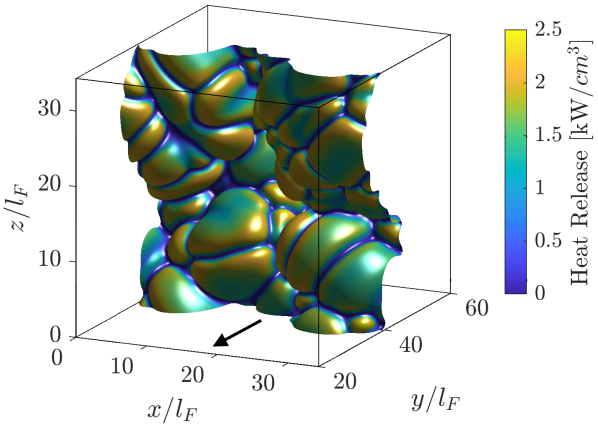

Figure 3: Snapshot of the flame surface area of the *LamUnstable* case colored by the heat release. The flame surface area is defined by an iso-surface of progress variable at $C_{\mathrm{H_2}} = 0.8$. The initially flat flame is propagating towards an inlet and the flame propagation indicated by arrow.

which lead to the formation of small cellular structures and distinct cusps, yielding a strongly corrugated flame front.

2.2. Governing Equations and Numerical Methods

The flow is modeled by the reacting Navier-Stokes equations in the low-Mach limit [34]. The fluid is assumed to be an ideal gas and chemical reactions are modeled by the mechanism of Burke et al. [35] that contains 9 species and 46 reactions. The viscosity of the mixture is determined according to Wilke [36] and the species viscosities are determined according to kinetic theory [37]. The thermal conductivity of the species are computed according to Eucken [38] and the thermal conductivity of the mixture is evaluated according to Mathur et al. [39]. The species diffusivities D_{i} are determined from the thermal conductivity λ, the density ρ, and the specific heat capacity c_{p} as $D_{\mathrm{i}} = \lambda/(\rho c_{\mathrm{p}} \mathrm{Le}_{\mathrm{i}})$ by imposing spatially homogeneous species Lewis numbers Le_{i}. For cases *TurbUnstable* and *LamUnstable*, the Lewis numbers were taken from the burned gas region of a one-dimensional unstretched premixed flame. All Lewis numbers for these two cases are provided in Tab. A1 in the supplementary material. For the *TurbStable* case, all Lewis numbers were set to unity to suppress effects of differential diffusion. Following Zhou et al. [29] and Schlup et al. [30], molecular

diffusion due to the Soret effect is also included in the *TurbUnstable* and *LamUnstable* case, while the Soret effect is disregarded in the *TurbStable* case to enforce equal diffusivity of all scalars. A summary of the model for the Soret effect is provided by Schlup et al. [40]. For the species diffusion velocity appearing in the species and temperature equations, a velocity-correction approach [41] is applied to enforce mass conservation.

A semi-implicit finite difference code, based on the Crank-Nicolson time advancement scheme and an iterative predictor corrector scheme, is employed [42]. Spatial and temporal staggering is used to increase accuracy and stability. The Poisson equation for the pressure is solved by the preconditioned conjugate gradient HYPRE solver [43]. Momentum equations are discretized with a second order scheme. In the species and temperature equations, the convective term is discretized with a fifth order WENO scheme [44] and the diffusion operator is discretized with second order central differences. The temperature and species equations are advanced by utilizing Strang's operator splitting [45]. The time integration of the chemical source terms employs a time-implicit backward difference method, as implemented in the stiff ODE solver CVODE as part of the SUNDIALS suite [46].

The mesh of the *TurbUnstable* and *TurbStable* cases is uniform in the streamwise (x) and spanwise (z) directions with a resolution of about $\Delta_{x,z} = 70\mu$m and $\Delta_{x,z} = 35\mu$m for the *TurbUnstable* and *TurbStable* case, respectively. The same resolution is applied in the crosswise (y) direction in the center of the domain, defined by $|y| < 2.5H$, while a weak stretching of the grid is applied sufficiently far away from the flame by a hyperbolic tangent profile towards the domain boundaries. The number of grid points is displayed in Tab. 1 and the resolution is such that η is well resolved at all times. The thermal flame thickness is resolved by ten grid points such that the laminar flame speed, heat release, temperature, and species profiles of a one-dimensional premixed unstretched flame computed by FlameMaster [47] are recovered adequately. It is worth noting that an additional simulation of the *TurbUnstable* case has been performed with half the resolution, but no significant effects on the flame statistics and drawn conclusions are observed as shown in Sec. 4 of the supplementary material. The timestep is controlled by the Courant-Friedrichs-Lewy (CFL) condition based on the local velocities and a maximum CFL number of 0.5 is allowed. This yields timesteps of approximately $\Delta t \approx 0.55$ μs in the *TurbUnstable* case and $\Delta t \approx 0.22$ μs in the *TurbStable* case, respectively.

The mesh of the *LamUnstable* case is equidistant in x- and z-direction with a resolution of $\Delta = 70$ μm and for numerical efficiency, a constant mesh size with a resolution of $\Delta = 70$ μm is chosen in y-direction for $20 < y/l_F < 70$, while a weakly stretched mesh is applied sufficiently far away from the flame towards the inlet and outlet. Thus, the thermal flame thickness is adequately resolved by ten grid points and a timestep of $\Delta t = 4$ μs is applied. The simulation of the *LamUnstable* case features a computational mesh of $352 \times 695 \times 352$ grid cells and an overall run time of $35\tau_F$, where $\tau_F = l_F/s_L$ is the flame time. Statistics are collected after a statistically steady state is reached at $20\tau_F$.

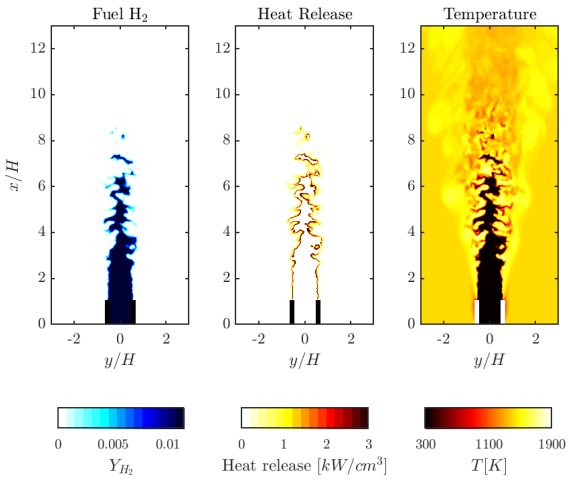

(a) *TurbUnstable* case

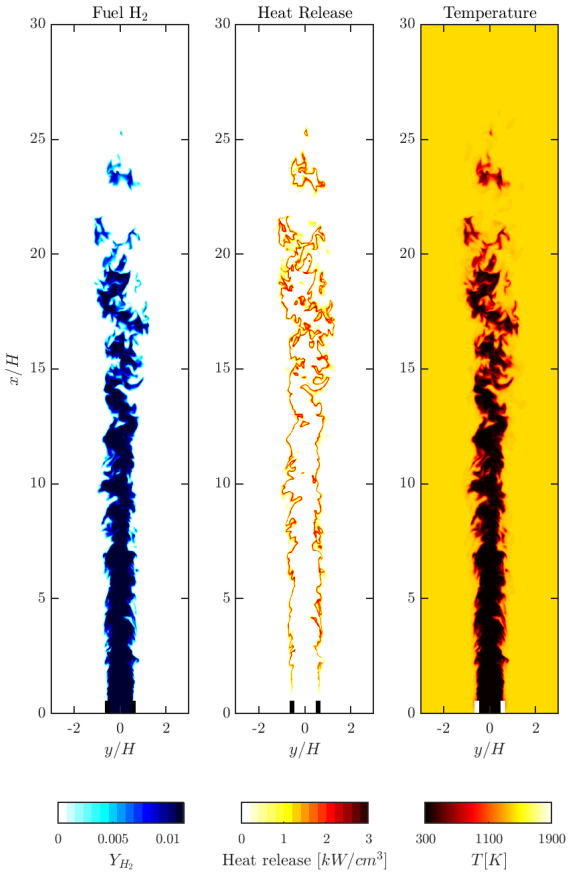

(b) *TurbStable* case

Figure 4: Instantaneous snapshots of the fuel mass fraction, heat release rate, and temperature for the two turbulent flames.

3. Results & Discussion

Fig. 4 shows a comparison of the *TurbUnstable* and *TurbStable* cases for the hydrogen mass fraction, the heat release,

and the temperature field. The *TurbUnstable* flame possesses a significantly shorter height if measured in terms of the slot width H, indicating a higher turbulent flame speed compared to the *TurbStable* case. The flames' visual appearance also differs significantly. The *TurbStable* case possesses an intact flame front with a relatively constant heat release while the heat release in the *TurbUnstable* case reveals strong fluctuations marked by local extinction and regions of intense burning. In the *TurbUnstable* flame, super-adiabatic temperatures are observed in the burned gas behind the flame front (note that the coflow temperature is set to the adiabatic temperature), which does not occur in the *TurbStable* case. Both features have been similarly observed by Aspden et al. [22] in homogeneous isotropic turbulence and also in the *LamUnstable* case and are clear markers of thermodiffusive instabilities [12].

3.1. Definitions and Assessment of Entrainment Effects

A progress variable based on the hydrogen mass fraction is defined as

$$C_{\mathrm{H_2}} = 1 - Y_{\mathrm{H_2}}/Y_{\mathrm{H_2,u}}, \tag{4}$$

where $Y_{\mathrm{H_2,u}}$ refers to the value in the unburned gas. An example for the instantaneous distribution of the progress variable for the case *TurbUnstable* is shown in Fig. 5a.

While a progress variable could be also defined based on the mass fraction of water, Berger et al. [12] showed that such a progress variable possesses sub- and super-equilibrium values in the post flame region similar to the temperature, so unity values that typically define the burned gas are ambiguous. The sub-unity values in the post flame region also lead to long tails of the iso-surfaces of the water mass fraction into the burned gas, leading to a spurious increase of the flame surface area; further details are provided in Berger et al. [12]. As the determination of flame surface area and combustion process are well posed for a hydrogen-based progress variable, $C_{\mathrm{H_2}}$ is used in the following.

The super-equilibrium values of temperature and combustion products, such as water, are illustrated in Fig. 5b for the mass fraction of water, which is normalized by the equilibrium value $Y_{\mathrm{H_2O,b}}$. For the *TurbUnstable* case, the variation of the local equivalence ratio is expressed in Fig. 5c by means of the mixture fraction Z, which is defined by the Bilger formula [48] as

$$Z = \frac{Z_{\mathrm{H}} + \nu(Y_{\mathrm{O_2,air}} - Z_{\mathrm{O}})}{1 + \nu Y_{\mathrm{O_2,air}}}. \tag{5}$$

The stoichiometric coefficient ν is defined by the ratio of the molar masses of oxygen and hydrogen as $\nu = 2M_{\mathrm{H_2}}/M_{\mathrm{O_2}}$, Z_{H} and Z_{O} represent the element mass fractions of hydrogen and oxygen, and $Y_{\mathrm{O_2,air}}$ is the mass fraction of oxygen in air. The variations of mixture fraction are clearly visible in Fig. 5c, where locally higher and smaller values of Z are seen in the flame front compared to the value of $Z_{\mathrm{eq}} = 0.012$ in the fully mixed equilibrium region. However, it is worth noting that the variations of mixture fraction do not exceed the stoichiometric value, which is $Z_{\mathrm{st}} = 0.028$, such that hydrogen is always fully consumed. Hence, the progress variable $C_{\mathrm{H_2}}$ always reaches unity values in the burned gas as visible in Fig. 5a. The fluctuations of the local equivalence ratio in thermodiffusively unstable flames have been similarly observed in laminar flames [12, 49] and by Aspden et al. [22] in homogeneous turbulence. While there are positive and negative fluctuations of mixture fraction within the flame front, it is interesting to note that in the post flame region before the coflow is reached, the values of mixture fraction and the mass fraction of water are seen to be higher than the value in the unburned gas or coflow, respectively; this observation will be discussed in detail later. Variations of mixture fraction do not occur in the *TurbStable* case as the effects of differential diffusion are suppressed. In particular, the water-based and hydrogen-based progress variables are almost identical in this case as all scalars possess equal diffusivities.

It has been shown that mixing and entrainment of coflow might have an effect on the flame dynamics [50, 51], so it is important to assess their presence in the two turbulent flames. For this, an additional transport equation for a passive non-reactive scalar ξ, whose diffusion is equal to the thermal diffusivity, has been solved in both turbulent cases. The value of ξ is set to $\xi = 1$ at the central jet inlet and to $\xi = 0$ at the coflow boundary conditions. Thus, the scalar ξ corresponds to a mixture fraction that indicates the mixing between the coflow and the central jet, but should not be confused with the previously introduced mixture fraction Z that is based on the element mass fraction and indicates the local equivalence ratio. Fig. 6 shows the conditional mean of ξ with respect to progress variable at different heights above the burner, where L_{Flame} is the flame height of each case, which is based on the fuel flux and will be defined in the next section. While close to the inlet for the *TurbStable* case, high values of the progress variable show some minor interaction with the coflow and lead to a reduction of ξ, the other axial positions are characterized by $\xi \approx 1$ for all values of the progress variable. Thus, the flames are located in regions, where entrainment is not relevant and additional information is provided in Sec. 5 of the supplementary material. Note that the significant reduction of ξ at $C_{\mathrm{H_2}} = 1$ is expected as these states represent the post flame region and the coflow. Thus, the effects of dilution and preheating of the unburned gas prior to combustion may be neglected for the present analyses.

3.2. Analysis of Turbulent Flame Speed

Fig. 7a shows the fuel consumption along the axial direction by means of the axial fuel flux $\mathcal{F}$, which is defined as

$$\mathcal{F} = \frac{1}{\rho_{\mathrm{u}} U H Y_{\mathrm{H_2,u}}} \cdot \int \langle \rho u_{\mathrm{x}} Y_{\mathrm{H_2}} \rangle \mathrm{d}y. \tag{6}$$

The operator $\langle ... \rangle$ represents averaging in time and the statistically homogeneous z-direction and ρ, u_{x}, and $Y_{\mathrm{H_2}}$ are the local density, axial velocity, and hydrogen mass fraction. For convenience, the fuel flux $\mathcal{F}$ is normalized by its value at the inlet, which is given by the bulk velocity U, the slot width H, the unburned gas density ρ_u, and the hydrogen mass fraction in the unburned gas $Y_{\mathrm{H_2,u}}$. Consistent with the visual appearance in Fig. 4, the fuel is consumed much faster in the *TurbUnstable* case, yielding a significantly shorter flame. This is caused by a

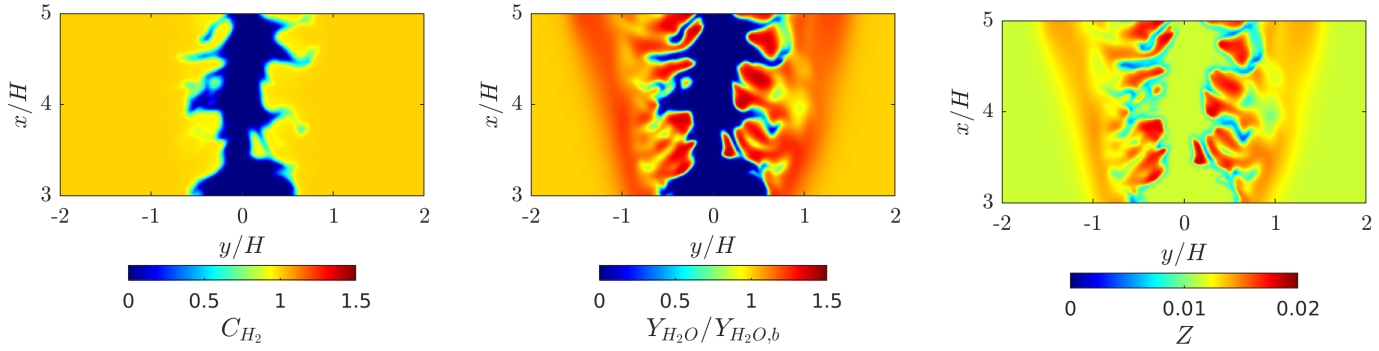

(a) Progress variable $C_{\mathrm{H_2}}$

(b) Mass fraction of water $Y_{\mathrm{H_2O}}$ normalized by its equilibrium value $Y_{\mathrm{H_2O,b}}$

(c) Mixture fraction Z

Figure 5: *TurbUnstable* case: Instantaneous snapshot of the hydrogen-based progress variable $C_{\mathrm{H_2}}$, the water mass fraction $Y_{\mathrm{H_2O}}$ normalized by its equilibrium value $Y_{\mathrm{H_2O,b}}$, and mixture fraction Z.

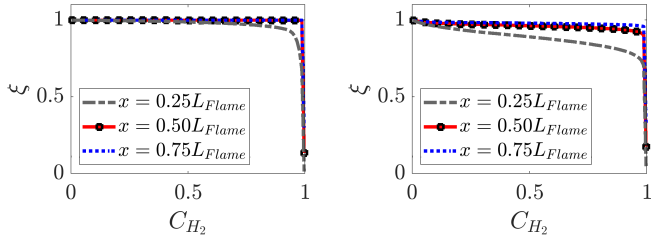

(a) Case *TurbUnstable*

(b) Case *TurbStable*

Figure 6: Conditional average of the mixture fraction ξ, which indicates the mixing of the central jet with the coflow, with respect to progress variable $C_{\mathrm{H_2}}$ at different heights above the burner for the two turbulent flames.

significantly higher fuel consumption rate in the *TurbUnstable* case as discussed in the following. The flame height L_{Flame} in Tab. 1 is determined from the location, where $\mathcal{F} = 0.01$.

Following Attili et al. [52], it is appropriate to define a local turbulent flame speed that evolves in the streamwise direction due to the strong spatial inhomogeneity of the flow in the streamwise direction x. It is defined by the consumption speed s_{c} as

$$s_{\mathrm{c}} = -\frac{1}{\rho_{\mathrm{u}} A_0 Y_{\mathrm{H_2,u}}} \int_{\mathcal{V}} \dot{\omega}_{\mathrm{H_2}} \mathrm{d}V. \tag{7}$$

Here, A_0 refers to a reference flame surface area that is discussed in the following, and $\dot{\omega}_{\mathrm{H_2}}$ represents the fuel consumption rate due to chemical reactions, which is integrated over a volume $\mathcal{V}$. For the volumetric integral in Eq. 7, the streamwise direction is divided in a number of equally sized volumes $\mathcal{V}^*$. Each of these extends along the entire spanwise z and crosswise direction y. The size of these volumes in the streamwise direction is as small as possible but finite such that converged statistics are obtained. An instantaneous flame surface area $A_{\mathrm{inst.}}$ in each volume $\mathcal{V}^*$ is determined based on the progress variable $C_{\mathrm{H_2}}$ according to [53]

$$A_{\mathrm{inst.}} = \int_{\mathcal{V}} \delta(C_{\mathrm{H_2}} - C_0) |\nabla C_{\mathrm{H_2}}| \mathrm{d}V. \tag{8}$$

The flame sheet is defined by $C_0 = 0.8$, which is close to the most reactive iso-surface in both flames, but similar conclusions are obtained for other definitions of the flame sheet as shown in Fig. A6 in the supplementary material. The Dirac δ-function is defined by a top-hat function with a sufficiently small width of $\Delta C = 0.05$. The temporal average of $A_{\mathrm{inst.}}$ yields the turbulent flame surface area A. The reference flame surface area A_0 represents the surface area of the Favre-averaged progress variable field defined by $\widetilde{C_{\mathrm{H_2}}} = C_0$.

For the *TurbUnstable* and *TurbStable* cases, Fig. 7 shows the normalized consumption speed $s_{\mathrm{c}}/s_{\mathrm{L}}$ along the streamwise direction x, where s_{L} is the burning velocity of a laminar unstretched flamelet, which is computed at the nominal equivalence ratio of $\phi = 0.4$ with the same diffusivity model as the corresponding turbulent case[1]. It is evident that the *TurbUnstable* flame features a significantly larger turbulent flame speed than the *TurbStable* case, reaching a peak value that is about 15 times larger than s_{L}, while a significantly smaller enhancement of the turbulent flame speed with a maximum value of $s_{\mathrm{c}}/s_{\mathrm{L}} \approx 5$ is obtained in the *TurbStable* case. To assess this large difference of the turbulent flame speed in the two flames, the latter can be decomposed into three components: the laminar unstretched burning velocity s_{L}, the surface area increase of the turbulent flame, which is the ratio of the turbulent and reference surface area A/A_0, and a stretch factor I_0, which accounts for variations of the flame structure, such as reactivity and local flame thickness, compared to a laminar unstretched flamelet. This yields the expression

$$s_{\mathrm{c}} = s_{\mathrm{L}} \frac{A}{A_0} I_0. \tag{9}$$

The contributions of surface area increase A/A_0 and the stretch factor I_0 are shown in Fig. 7. In both cases, the flame surface area increases towards the tip of the flame and a rapid de-

[1] Since the axial position of the tip of the average flame contour, defined by $\widetilde{C}_{\mathrm{H_2}} = C_0$, is different from the flame height L_{Flame}, defined by $\mathcal{F} = 0.01$, the curves in Fig. 7 end at $x < L_{\mathrm{Flame}}$.

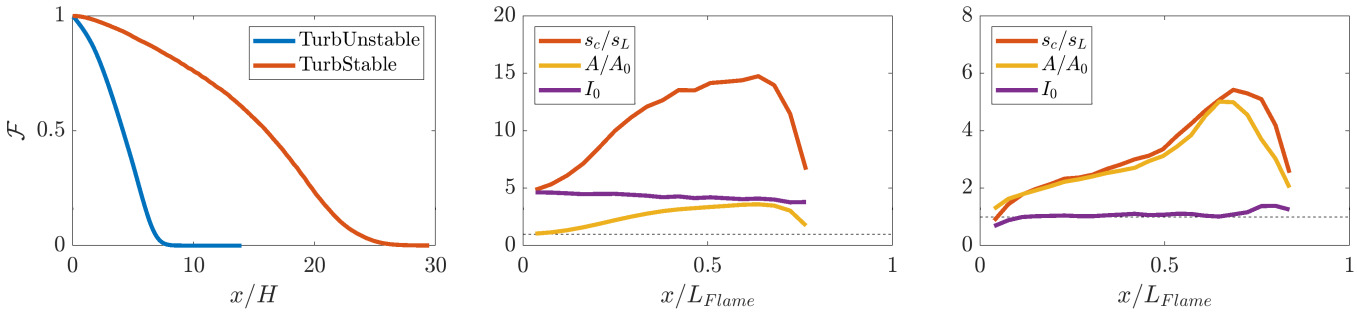

(a) Fuel flux $\mathcal{F}$ for both flames.

(b) Consumption speed decomposition for case *TurbUnstable*

(c) Consumption speed decomposition for case *TurbStable*

Figure 7: Fuel flux, consumption speed, surface area increase, and stretch factor at different heights above the burner for both turbulent flames.

struction of flame surface area is observed at the tip[2]. While the contribution of flame wrinkling appears to be similar in Fig. 7, as a maximum value of $A/A_0 \approx$ 4-5 is observed in both flames, it is worth noting that the *TurbUnstable* case features a significantly shorter flame. Thus, the mechanisms of flame surface area formation need to be assessed in greater detail in the following. Further, significantly different values of the stretch factor are observed in the two cases. In the *TurbStable* case, a unity stretch factor is observed indicating a local burning behavior that is close to an unstretched laminar flamelet and, hence, the increase of the turbulent flame speed can be only attributed to the increase of flame surface area. This is in agreement with the findings of Attili et al. [52], who showed that the increase of the turbulent flame speed in methane/air flames, which do not feature thermodiffusive instabilities, is almost only caused by flame wrinkling due to turbulence. On the contrary, the *TurbUnstable* case possesses a remarkably high stretch factor of $I_0 \approx 4$, which results in a significantly enhanced turbulent flame speed and, hence, a shorter flame. It is worth noting that the stretch factor in the turbulent *TurbUnstable* flame is larger compared to the value $I_0 = 2.6$ obtained in the *LamUnstable* case even though the two flames are performed at the same equivalence ratio, unburned temperature, and pressure. This enhancement of reactivity due to the presence of turbulence is a first indication of a synergistic effect of turbulence and thermodiffusive instabilities on the flame propagation and will be discussed in detail in the subsequent sections.

3.3. Generation and Destruction of Flame Surface Area

Based on the flame surface area density formalism, Vervisch et al. [53] defined a flame surface area density $\Sigma(\boldsymbol{x}, t)$ of a progress variable iso-surface at $C_{\mathrm{H_2}} = C_0$ per unit volume. $\Sigma(\boldsymbol{x}, t)$ is given by

$$\Sigma(\boldsymbol{x}, t) = \langle |\nabla C_{\mathrm{H_2}}| \delta(C_{\mathrm{H_2}} - C_0) \rangle. \tag{10}$$

It is worth noting that the flame surface area A within a certain volume $\mathcal{V}$ and the flame surface area density Σ are connected via

$$A = \int_{\mathcal{V}} \Sigma(\boldsymbol{x}, t) \mathrm{dV}. \tag{11}$$

For the flame surface area density $\Sigma(\boldsymbol{x}, t)$, a transport equation can be derived as [53]

$$\nabla \cdot \left[\langle \boldsymbol{u} + s_\mathrm{d} \boldsymbol{n} \rangle_\mathrm{S} \, \Sigma(\boldsymbol{x}, t) \right] = \langle K \rangle_\mathrm{S} \, \Sigma(\boldsymbol{x}, t), \tag{12}$$

where K is the local stretch rate, s_d is the flame displacement speed, $\langle ... \rangle_\mathrm{S}$ represents surface-averaging, and the temporal derivative of $\Sigma(\boldsymbol{x}, t)$ disappears due to the statistically stationary flame configuration in this work. The surface-average of a quantity Q is defined as

$$\langle Q \rangle_\mathrm{S} = \frac{\langle Q \, |\nabla C_{\mathrm{H_2}}| \, | C_0 \rangle}{\langle |\nabla C_{\mathrm{H_2}}| \, | C_0 \rangle}, \tag{13}$$

where $\langle ... | C_0 \rangle$ is the conditional average with respect to the value of the progress variable that defines the flame sheet. The stretch rate K depends on the flame curvature κ, the tangential strain rate K_S, and the flame displacement speed s_d. These parameters are defined as

$$K = \kappa s_\mathrm{d} + K_\mathrm{S}, \tag{14}$$

$$\kappa = \nabla \cdot \boldsymbol{n}, \tag{15}$$

$$K_\mathrm{S} = \nabla \cdot \boldsymbol{u} - \boldsymbol{n} \cdot \nabla \boldsymbol{u} \cdot \boldsymbol{n}, \tag{16}$$

where $\boldsymbol{n} = -\nabla C_{\mathrm{H_2}} / |\nabla C_{\mathrm{H_2}}|$ is the flame normal vector that points towards the unburned gas and $\boldsymbol{u}$ is the gas velocity. The flame displacement speed s_d is given by [54]

$$s_\mathrm{d} = \frac{1}{|\nabla C_{\mathrm{H_2}}|} \left(\frac{\partial C_{\mathrm{H_2}}}{\partial t} + \boldsymbol{u} \cdot \nabla C_{\mathrm{H_2}} \right) \tag{17}$$

The left hand side of Eq. 12 describes the convection of the flame sheet, whose propagation velocity $\boldsymbol{w}$ is given by $\boldsymbol{w} = \boldsymbol{u} + s_\mathrm{d} \boldsymbol{n}$ [54], and the right hand side term represents a source term that is proportional to the stretch rate K, which according to Eq. 14 can be decomposed into contributions of strain rate K_S and the term κs_d, which is referred to as 'curvature term'.

Fig. 8 shows the surface-averaged stretch rate, strain rate, and curvature term for both turbulent flames. Consistent with the

[2]Note that a detailed analysis of the flame tip dynamics, which feature flame-flame interactions, is outside the scope of this work as the present study focuses on the analysis of the flame-turbulence interactions.

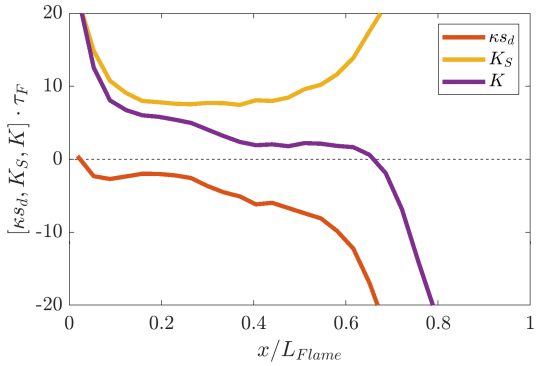

(a) Case *TurbUnstable*

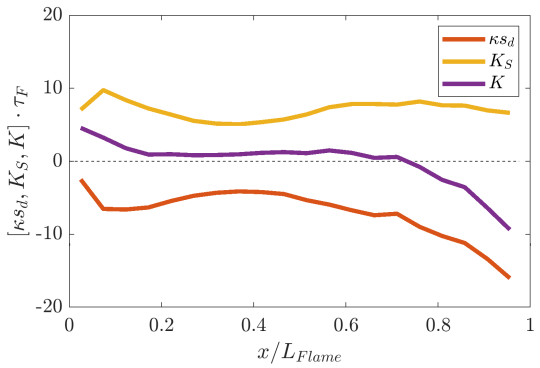

(b) Case *TurbStable*

Figure 8: Surface-averaged stretch, strain rate, and curvature term at different heights above the burner and normalized by the flame time τ_F.

increase of flame surface area in axial direction in Fig. 7, the surface-averaged stretch rate is positive for both cases until the tip of the flame is reached, leading to a monotonic increase of flame surface area. At the tip, a strong destruction of flame surface area due to large negative stretch rates is observed. For both cases, the mean positive strain rate is seen to generate flame surface area while the curvature term is mostly negative and leads to a destruction of flame surface area. In the following, it will be shown that the flame surface area generation by the mean positive strain rate is dictated by turbulence and is not affected by the thermodiffusive instabilities, while the dynamics of the curvature term are closely linked to the interactions of the thermodiffusive instabilities and turbulence.

3.3.1. Analysis of Strain Rate

The positive tangential strain rates are consistent with several earlier studies of turbulent premixed flames [55–58]. The tangential strain rate K_S is generally found to be positive for both non-reactive and reactive turbulent flows and remains mostly unaffected by a flame's heat release. This is in contrast to the normal strain rate, which is affected by the heat release and consequently also by the effects of differential diffusion that sensitively affect the heat release [55]. If normalizing the strain rate by the Kolmogorov time scale τ_η, a value of $\langle K_S \rangle_S \tau_\eta \approx 0.28$ has been reported by Rutland et al. [56] for turbulent premixed flames in decaying homogeneous isotropic turbulence. Luca et al. [59], who studied turbulent premixed methane/air flames in a slot burner configuration at different jet Reynolds numbers up to $Re = 22,400$ and the same Karlovitz number as this study, observed an almost constant value of $\langle K_S \rangle_S \tau_\eta \approx 0.24$ over the different flame heights and also showed that this value is independent of the Reynolds number if scaled with τ_η. The Kolmogorov time scale is determined as $\tau_\eta = (\overline{\nu}/\widetilde{\epsilon})^{1/2}$ [33]. Thus, Fig. 9 shows the surface-averaged stretch rate, strain rate, and curvature term normalized by the Kolmogorov time scale τ_η. Consistent with the findings of Luca et al. [59] and Rutland et al. [56], an almost constant value of the surface-averaged strain rate is obtained over the height of the flame if normalized by τ_η, yielding a value of $\langle K_S \rangle_S \tau_\eta \approx 0.28$ for the two turbulent flames. Further, Fig. 10 shows the probability density function (PDF) of the strain rate that is normalized by τ_F and τ_η at different axial positions for the *TurbUnstable* case. Only if normalized by the Kolmogorov time scale τ_η, the PDFs become self-similar indicating that the strain rate is strongly correlated with the small scales of the turbulent flow. The PDFs of the *TurbStable* case are shown in Fig. A7 in the supplementary material, but since τ_η is constant along the flame height both normalizations yield self-similar PDFs. Note that for the *TurbUnstable* case, τ_η decreases towards the flame tip. This can be seen from Fig. 2, where an increase of Karlovitz number, which can be also defined as $Ka = \tau_F/\tau_\eta$, is seen. Hence, the consistency of $\langle K_S \rangle_S \tau_\eta$ with values obtained in flames that do not feature thermodiffusive instabilities and the self similarity of the PDF if normalized by τ_η suggest that surface area generation by strain rate is dominated by turbulence rather than a flame intrinsic mechanisms and, in particular, thermodiffusive instabilities.

3.3.2. Analysis of Curvature Term

Regarding the normalized curvature term in Fig. 9, a constant value is observed up to half of the flame height for the *TurbStable* case and then, a strong decrease of $\langle \kappa s_d \rangle_S \tau_\eta$ is seen close to the flame tip. This was similarly observed by Luca et al. [59] in the turbulent premixed methane/air slot burner flames. However, for the *TurbUnstable* case, the curvature term is not constant over the flame height irrespective of its normalization by τ_η or τ_F, giving a first indication that the underlying physics of the flame destruction mechanism are entirely different for this case. To assess the differences of the curvature term in the two flames, it is instructive to first qualitatively discuss its effects on the flame surface area formation and thereafter, the curvature term is analyzed by means of a statistical analysis. It will be shown that the curvature term possesses a distinctly different behavior in the two turbulent flames, which is directly linked to the presence of thermodiffusive instabilities. In particular, thermodiffusive instabilities are shown to generate characteristic tongue-like structure and a comparison of the *TurbUnstable* and *LamUnstable* case reveals that the generation of flame surface area by the thermodiffusive instability mechanism is even amplified in the *TurbUnstable* case due to the higher values of curvature in the turbulent environment.

To illustrate the differences of the curvature term, Figs. 11 and 12 show three-dimensional visualizations of the flame front for the two turbulent flames. The view is from the centerline of

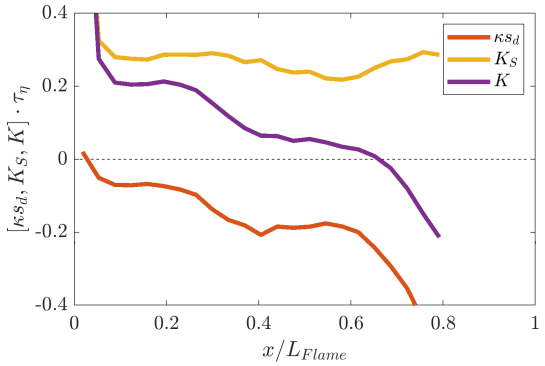

(a) Case *TurbUnstable*

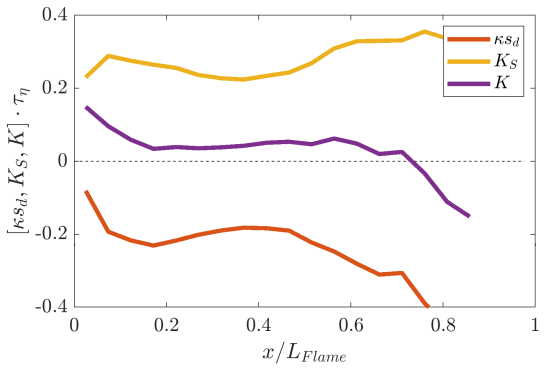

(b) Case *TurbStable*

Figure 9: Surface-averaged stretch, strain rate, and curvature term at different heights above the burner and normalized by the Kolmogorov time τ_η.

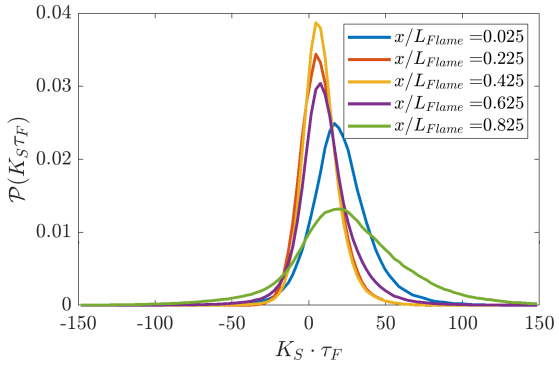

(a) Normalization by flame time τ_F

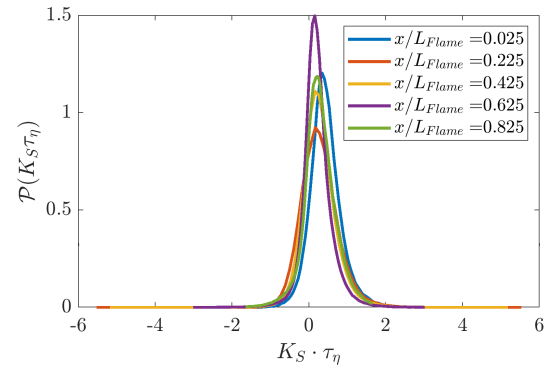

(b) Normalization by Kolmogorov time τ_η

Figure 10: *TurbUnstable* case: Different normalizations of the PDF of strain rate at different heights above the burner; the data for building the PDF have been weighted by $|\nabla C_{\mathrm{H_2}}|$ to be consistent with the surface-averages in Figs. 8 and 9.

the slot burner looking at the flame sheets from the unburned gas (the average flame propagation direction is indicated by an arrow). The flame sheet is colored by the stretch rate, the strain rate, the curvature term, the heat release, the mixture fraction, and the normalized flame displacement speed s_d^*, which is defined as

$$s_\mathrm{d}^* = \frac{\rho_\mathrm{iso} s_\mathrm{d}}{\rho_\mathrm{u}} \tag{18}$$

to compensate for the change of density in the flame, where ρ_iso is the density at the flame sheet. Hence, s_d^* would be equal to s_L for any iso-surface in an unstretched laminar flame.

In the *TurbUnstable* case, several finger- or tongue-like structures that are convexly shaped towards the unburned gas with large values of the stretch rate at their tip are formed. Since stretch acts as a source term for the flame surface area, the large positive values of stretch at the tip of the flame tongues lead to a further enlargement of these structures supporting their propagation into the unburned gas and are a clear marker of thermodiffusive instabilities. In contrast, the *TurbStable* case does not possess such recurring finger- or tongue-like structures and, in particular, the leading flame edges that are convexly curved towards the unburned gas are destroyed as negative values of stretch are seen at these locations. For both cases, large negative values of stretch are seen in the cusp regions and the large positive and negative values of stretch are closely linked to the curvature term, while the dependence of strain rate on the flame topology is less pronounced. It is worth noting that the tongue-like structures in the *TurbUnstable* case are similar to the flame fingers, which have been observed in laminar thermodiffusively unstable flames with large domain sizes [4, 12].

The remarkable difference of the curvature term at the tip of the flame edges and tongue-like structures in the turbulent flames is related to a different behavior of the flame displacement speed. The value of s_d is determined by the local reaction rate and the diffusive fluxes (note that in Eq. 17, s_d is evaluated from the left hand side of the progress variable transport equation, but could be also determined from the right hand side, which contains the reaction rate and the diffusive fluxes). Since the diffusive fluxes are proportional to curvature [60], they tend to reduce s_d in flame segments that are convexly curved towards the unburned gas and increase s_d in the cusp regions. In the *TurbStable* case, the heat release is almost constant along the flame sheet, so a reduction of s_d^*, which even yields negative values, is seen at the leading flame edges, while s_d^* is increased in the cusp regions. In contrast, the *TurbUnstable* case features strong variations of the heat release, which are caused by the differential diffusion of hydrogen. To highlight the effects of differential diffusion, Fig. 11 also shows the distribution of mixture fraction, whose values are enhanced at the tip of the flame tongue and diminished in the cusp regions. Thus, the

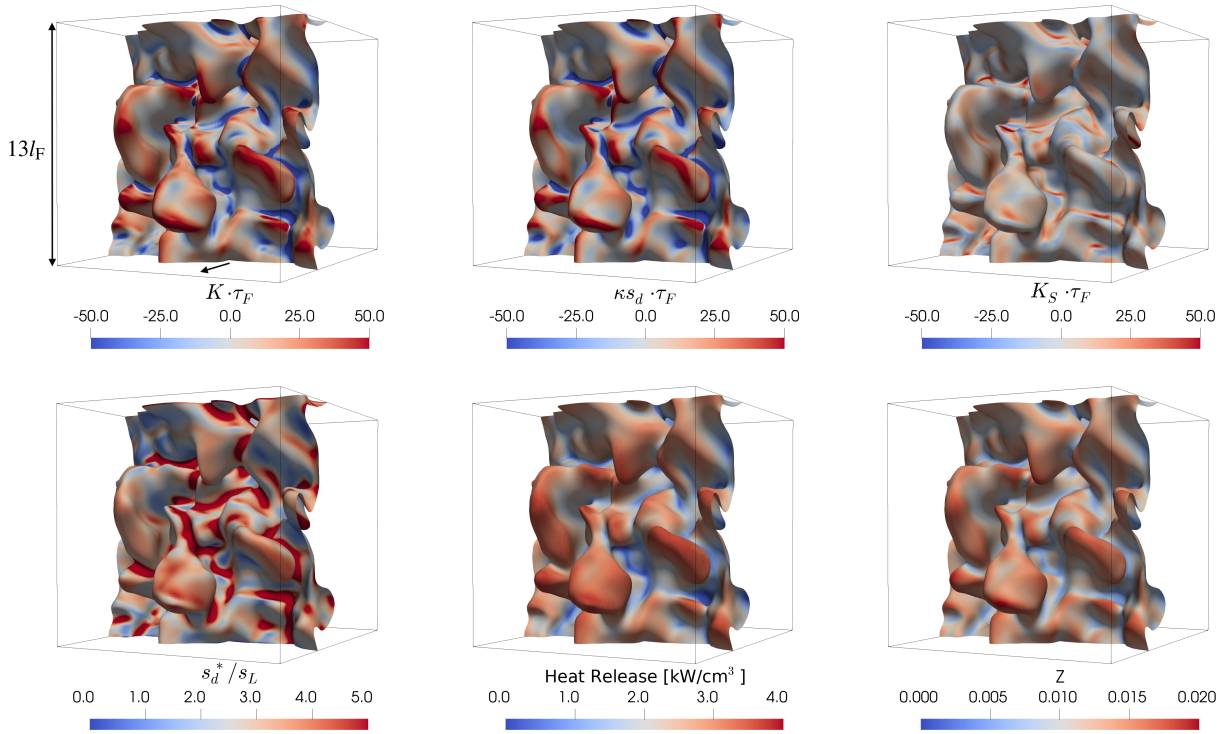

Figure 11: *TurbUnstable* case: Three-dimensional snapshots of the instantaneous flame front defined by $C_{H_2} = 0.8$ and colored by stretch, the curvature term, strain rate (left to right; top row), the normalized displacement speed, heat release, and mixture fraction (left to right; bottom row). The view is from the centerline of the slot burner looking at the flame sheets from the unburned gas (the average flame propagation direction is indicated by an arrow). Figures are taken at $x/H = 2.7$ above the nozzle.

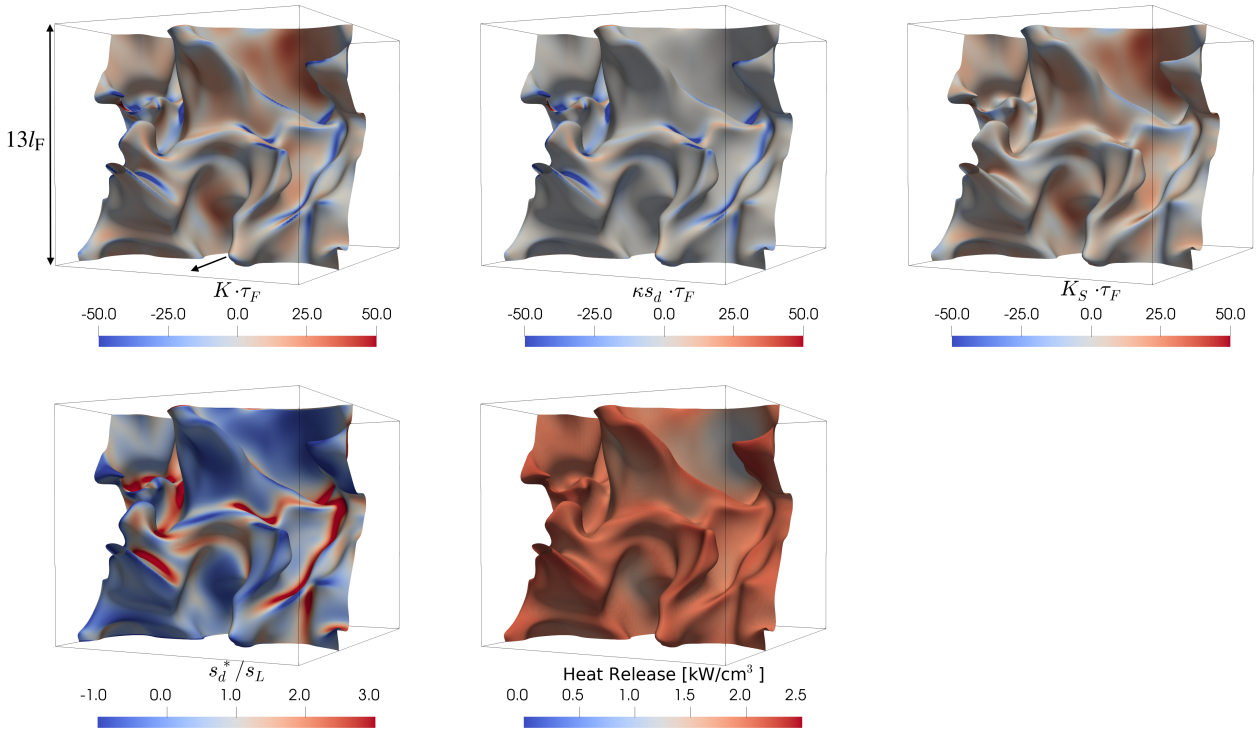

Figure 12: *TurbStable* case: Three-dimensional snapshots of the instantaneous flame front defined by $C_{H_2} = 0.8$ and colored by stretch, the curvature term, strain rate (left to right; top row), the normalized displacement speed, and heat release (left to right; bottom row). The view is from the centerline of the slot burner looking at the flame sheets from the unburned gas (the average flame propagation direction is indicated by an arrow). Figures are taken at $x/H = 9.5$ above the nozzle.

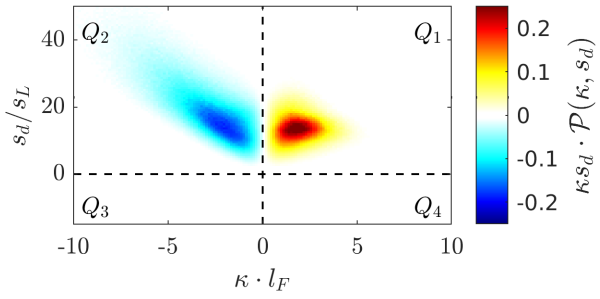

(a) Case *TurbUnstable*

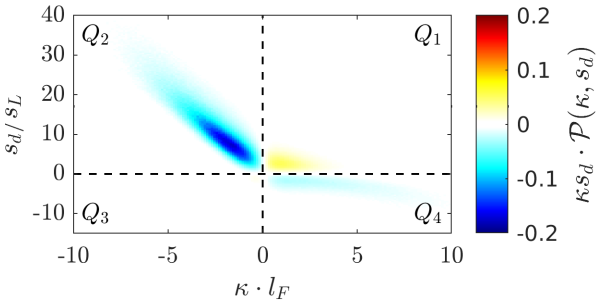

(b) Case *TurbStable*

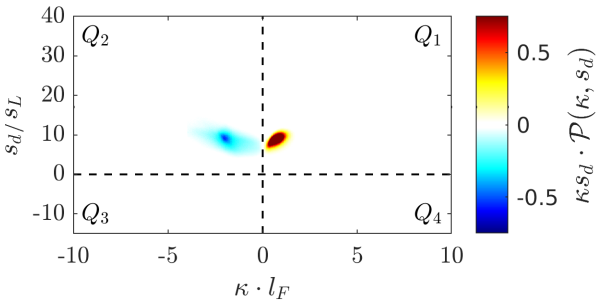

(c) Case *LamUnstable*

Figure 13: Analysis of the curvature term by means of the joint distribution $\mathcal{P}(\kappa, s_\mathrm{d})$ times κs_d. Q_i indicate the different quadrants of the distribution.

impact of the diffusive term is more than compensated by the increase of reaction rates at the tip of the flame tongues leading to a significantly increased value of s_d^*. In the cusp regions of the *TurbUnstable* case, where the heat release vanishes, still an increase of s_d^* is seen similar to the *TurbStable* case indicating that the diffusive fluxes dominate the flame propagation in the cusp regions of both flames irrespective of the variations of the heat release in the *TurbUnstable* case. Hence, the curvature term leads to flame surface area destruction in the cusp regions in both flames, while surface area is generated at the tip of flame tongues in the *TurbUnstable* case and destroyed at the leading edges of the *TurbStable* case.

To quantify the differences among the curvature terms in the two cases, the joint distribution $\mathcal{P}(\kappa, s_\mathrm{d})$ of curvature κ and displacement speed s_d is studied in the following. By means of $\mathcal{P}(\kappa, s_\mathrm{d})$, the surface-averages in Fig. 8 can be expressed as

$$\langle \kappa s_\mathrm{d} \rangle_\mathrm{S} = \int \kappa s_\mathrm{d} \mathcal{P}(\kappa, s_\mathrm{d}) \, \mathrm{d}\kappa \mathrm{d}s_\mathrm{d}, \tag{19}$$

where the joint distribution $\mathcal{P}(\kappa, s_\mathrm{d})$ has been determined by

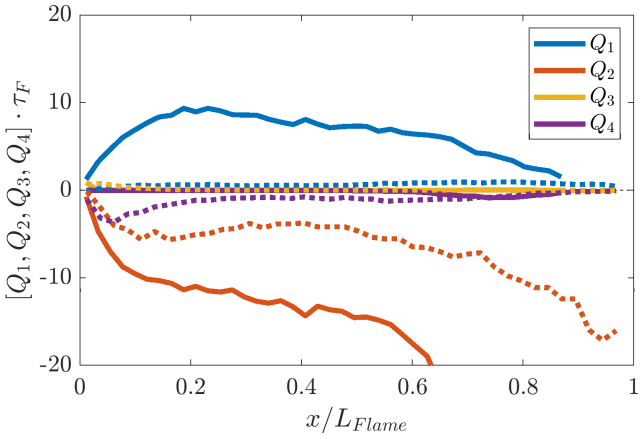

Figure 14: Contributions of each quadrant Q_i to the surface-averaged curvature term at different heights above the burner for the *TurbUnstable* case (solid lines) and *TurbStable* case (dashed lines)

considering $|\nabla C_{\mathrm{H_2}}|$ as a weighting factor to ensure consistency with the surface-averages. Fig. 13 shows the joint distribution $\mathcal{P}(\kappa, s_\mathrm{d})$ multiplied by κs_d for both cases to highlight the positions in the κ-s_d-space that have a relevant contribution to the integral in Eq. 19. The statistics of $\mathcal{P}(\kappa, s_\mathrm{d})$ in Fig. 13 are taken at half of the flame height for the two flames, but, as shown in Figs. A12 and A13 the supplementary material, no significant differences are observed at other axial locations. The curvature term can be split into four characteristic contributions that are given by the four different quadrants Q_i in Fig. 13, for which κ and s_d possess either positive or negative values. Contributions from quadrant Q_1 and Q_3 lead to an increase of flame surface area, since $\kappa s_\mathrm{d} > 0$, and contributions from quadrant Q_2 and Q_4 lead to a destruction of flame surface area, since $\kappa s_\mathrm{d} < 0$. Quadrant Q_1 represents convexly curved flame segments that propagate into the unburned gas (e.g., the tip of the flame tongues in the *TurbUnstable* case). In Q_2, the flame is concavely curved with a positive propagation towards the unburned gas (e.g. the cusp regions), whereas in Q_3 and Q_4, the flame possess a negative propagation (e.g. the leading flame edges in the *TurbStable* case are located in Q_4). Consistent with the three-dimensional visualizations in Figs. 11 and 12, surface area consumption in the second quadrant Q_2, where the flame corrugations are flattened due to the strong diffusion in the cusp regions, has an equally significant contribution for both cases. This is similarly seen in the *LamUnstable* case with an overall smaller contribution as less negative curvature values are obtained in this case.

For the quadrant Q_1, a significant contribution exists in the *TurbUnstable* and *LamUnstable* cases, which corresponds to the aforementioned surface area increase due to the propagation of the flame tongues into the unburned gas and is a distinct marker of thermodiffusive instabilities. In contrast, in the *TurbStable* case, only a very minor contribution is seen in quadrant Q_1 and also a small contribution of quadrant Q_4 appears, which corresponds to the destruction of surface area at the leading edges that are convexly curved towards the unburned gas. This behavior of the *TurbStable* case is very similar

to the methane/air flames studied by Luca et al. [32], where the contribution of quadrant Q_2 is dominant and the contribution of quadrant Q_1 is much less pronounced.

For the turbulent flames, Fig. 14 shows the contribution of each quadrant over the flame height, which, for example, for the first quadrant Q_1 is defined as

$$\langle \kappa s_\mathrm{d} \rangle_\mathrm{S}^{Q_1} = \int_0^\infty \int_0^\infty \kappa s_\mathrm{d} \mathcal{P}(\kappa, s_\mathrm{d})\, \mathrm{d}\kappa \mathrm{d}s_\mathrm{d}. \tag{20}$$

From Fig. 14, it is evident that the *TurbUnstable* case possesses a large contribution of the first quadrant to the overall curvature term, which is missing in the *TurbStable* case and also in the methane/air flames of Luca et al. [32] and is a clear marker of the presence of thermodiffusive instabilities. The surface area destruction by the second quadrant Q_2 is of similar importance in both flames, indicating that this mechanism is not related to the thermodiffusive instability mechanism while the contributions from the other quadrants are negligible.

Several similarities are seen among the *TurbUnstable* and *LamUnstable* cases, e.g., only contributions from quadrants Q_1 and Q_2 are significant in both cases. However, in the *LamUnstable* case, they are significantly smaller compared to the *TurbUnstable* case, which is linked to the significantly smaller values of curvature and the flame displacement speed in the *LamUnstable* case. Hence, as turbulence enhances the curvature fluctuations, which is further discussed in the following, and the flame's response in terms of the flame displacement speed in the *TurbUnstable* case, it leads to an amplification of the flame surface area destruction in the quadrant Q_2, but also enhances surface area generation in the quadrant Q_1, indicating a synergistic interaction with the thermodiffusive instability mechanism.

3.4. Flame State and Reaction Rates

Generally, the consumption speed of a turbulent flame can be enhanced by an increase of flame surface area or by variations of the flame's structure, i.e. variations of the reactivity or the flame thickness, which is accounted for by the stretch factor I_0 in Eq. 7. The underlying processes leading to the significantly increased super-unity value of I_0 in Fig. 7 for the *TurbUnstable* case are investigated in this section. All statistics of the *TurbUnstable* and *TurbStable* case are presented at half of the flame height, but no significant change of statistics is seen for other axial positions. The respective figures at different flame heights are provided in Sec. 10 of the supplementary material.

3.4.1. Mixture Fraction Fluctuations

The joint distribution of the progress variable source term $\dot{\omega}_\mathrm{C}$, which is defined as

$$\dot{\omega}_\mathrm{C} = -\dot{\omega}_{\mathrm{H}_2} / Y_{\mathrm{H}_{2,\mathrm{u}}}, \tag{21}$$

and C_{H_2} is shown in Fig. 15 for the two turbulent flames. Additionally, the unstretched laminar flamelets at $\phi = 0.4$, $T_\mathrm{u} = 298\mathrm{K}$, and $p = 1\mathrm{bar}$ that use the same diffusivity models as the *TurbUnstable* and *TurbStable* cases, respectively, are shown. While the source term of the *TurbStable* case follows closely

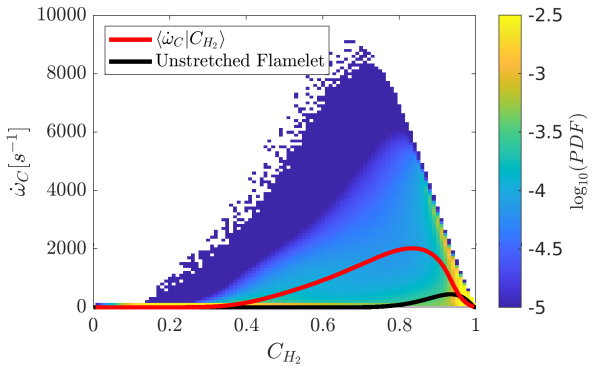

(a) Case *TurbUnstable*

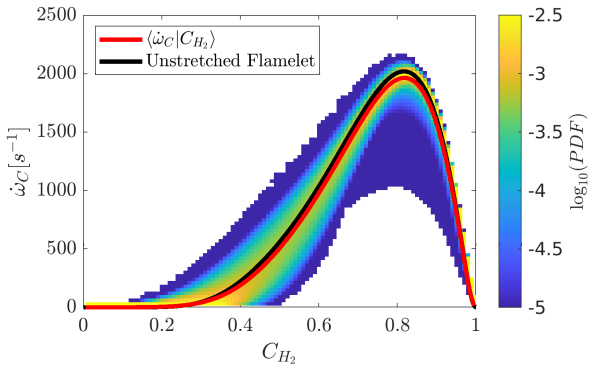

(b) Case *TurbStable*

Figure 15: Joint distribution of the source term $\dot{\omega}_\mathrm{C}$ and the progress variable C_{H_2}. Red lines represent the conditional mean and the black line corresponds to the unstretched laminar flamelet.

the values of the laminar unstretched flamelet, the source term of the *TurbUnstable* case reveals a strong scatter due to the strong variations of the local equivalence ratio. Hence, an adequate parametrization of the local flame state needs to include the mixture fraction Z, defined in Eq. 5, to account for the fluctuations of the local equivalence ratio.

To highlight the improvement of flame state parametrization of case *TurbUnstable* if mixture fraction is included, an optimal estimator analysis [61, 62] has been performed. In such an analysis, the capability of a set of parameters $\boldsymbol{\psi}$, e.g. $\boldsymbol{\psi} = [C_{\mathrm{H}_2}, Z]$, to parametrize a target quantity Q, e.g. $Q = \dot{\omega}_\mathrm{C}$, is quantified by an error norm referred to as irreducible error. In particu-

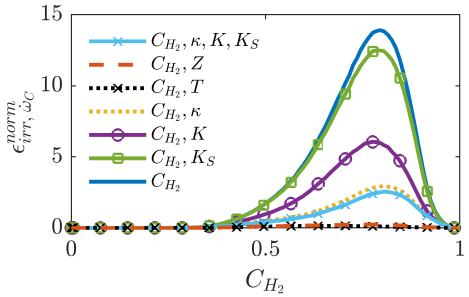

Figure 16: *TurbUnstable* case: Irreducible errors of $\dot{\omega}_\mathrm{C}$ if parametrized by different sets of parameters.

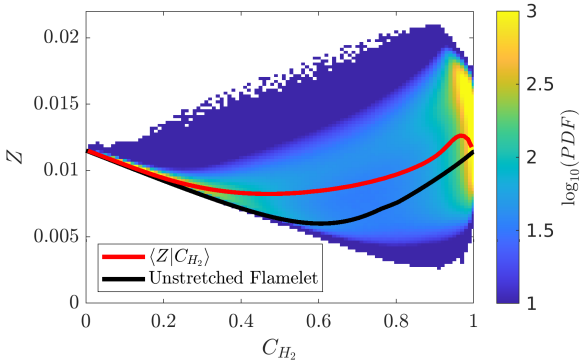

(a) *TurbUnstable* case

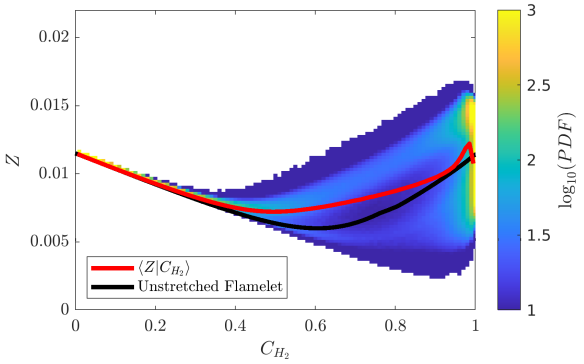

(b) *LamUnstable* case

Figure 17: Joint PDF of progress variable and mixture fraction $\mathcal{P}(C_{H_2}, Z)$.

lar, the amount of scatter of Q with respect to the conditional mean $\langle Q|\boldsymbol{\psi}\rangle$ is measured by the quadratic error norm. Thus, the parametrization is good if small irreducible errors are observed. In the following, the irreducible errors are conditionally averaged with respect to progress variable yielding

$$\epsilon^2_{\text{irr},\,\dot{\omega}_C} = \langle\, (\dot{\omega}_C - \langle\dot{\omega}_C|\boldsymbol{\psi}\rangle)^2 \mid C_{H_2}\,\rangle. \tag{22}$$

For reference, the conditionally averaged irreducible error is normalized by the maximum value of $\dot{\omega}_C^{\text{Flamelet}}$ in the unstretched flamelet yielding

$$\epsilon^{\text{norm}}_{\text{irr},\,\dot{\omega}_C} = \frac{\epsilon^2_{\text{irr}}}{\max(\dot{\omega}_C^{\text{Flamelet}})^2}. \tag{23}$$

Fig. 16 shows the irreducible errors if $\dot{\omega}_C$ is parametrized by different parameters and their combinations: The progress variable C_{H_2}, mixture fraction Z, the curvature of the flame front κ, the tangential strain rate K_S, the flame stretch K, and temperature T. Using only the progress variable for the parametrization, large irreducible errors are obtained, which is consistent with the large scatter visible in Fig. 15. A significant reduction of irreducible errors is seen if progress variable and mixture fraction are used since Z accounts for the variations of the local equivalence ratio. Using any of the parameters K, K_S, κ or all of them does not improve the parametrization as much as using mixture fraction in addition to progress variable. This indicates

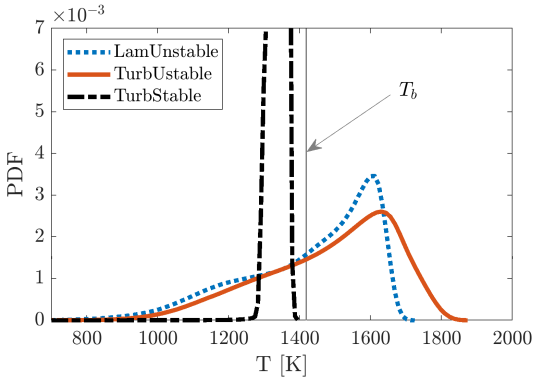

Figure 18: Temperature distribution in the post flame region for all three cases. Statistics are collected for $0.95 < C_{H_2} < 0.99$ and the adiabatic flame temperature or all cases is $T_b = 1418$K.

that $\dot{\omega}_C$ is not only determined by the instantaneous values of K, K_S, or κ, which represent the topology and local environment of the flame and whose variation causes the differential diffusion of hydrogen lateral to the flame front, but possibly also by their temporal evolution as suggested by Klimenko [63]. In contrast, the local value of mixture fraction represents the result rather than the cause of differential diffusion and, hence, yields a significantly improved parametrization of $\dot{\omega}_C$. It is worth noting that a similar good parametrization can be achieved if using temperature and progress variable, as similar to mixture fraction, one coordinate describes the combustion progress and the other one the effects due to differential diffusion. A similar analysis with the same conclusions has been provided for laminar thermodiffusively unstable flames by Berger et al. [12].

Fig. 17a shows the joint distribution of the progress variable C_{H_2} and mixture fraction Z for case *TurbUnstable*. To assess the impact of turbulence on the local flame state, the same joint distribution is also shown for case *LamUnstable* in Fig. 17b. However, the fluctuations of Z are significantly enhanced in the turbulent case and the average mixture fraction $\langle Z|C_{H_2}\rangle$ is significantly above the flamelet solution in the turbulent case, while it is closer to the flamelet solution in the *LamUnstable* case. As will be shown, the large mixture fraction fluctuations in the turbulent flame arise from the significantly higher fluctuations of flame front curvature in the *TurbUnstable* case compared to the *LamUnstable* case and the differences of the conditional means is linked to an enhanced mean strain due to turbulence in the *TurbUnstable* case.

The enhanced fluctuations of mixture fraction in the turbulent flow compared with the laminar flow also lead to enhanced fluctuations of the combustion products, e.g. the water mass fraction, and temperature in the burned gas. This is illustrated in Fig. 18, which shows the distribution of temperature in the post flame region, defined by $0.95 < C_{H_2} < 0.99$ (the upper value is not set to unity to exclude the coflow in the turbulent flames or regions far away from the flame front in the *LamUnstable* case). While a narrow distribution of temperature is seen in the *TurbStable* case, broad distributions with superadiabatic temperatures are seen for the two other flames similar to observations in previous works [22, 64]. The distribution of

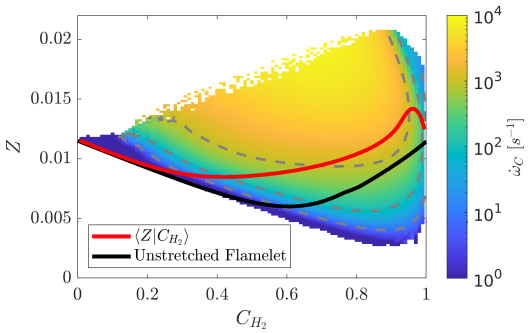

(a) *TurbUnstable* case

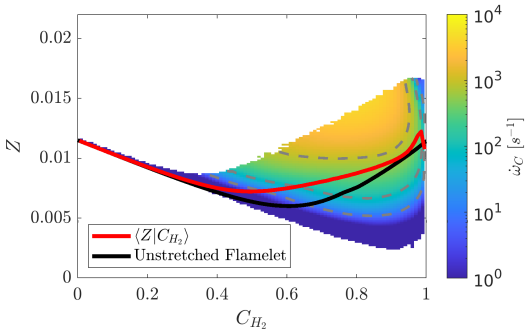

(b) *LamUnstable* case

Figure 19: Conditionally averaged source term $\dot{\omega}_C$ with respect to progress variable and mixture fraction including the conditional average $\langle Z|C_{H_2}\rangle$ (red line) and the solution of an unstretched laminar flamelet (black line). Grey dashed lines mark the values of $\dot{\omega}_C$ = 10, 100, and 1000 s^{-1} (grey dashed lines).

the *TurbUnstable* case features larger super-adiabatic temperatures up to 400K above the adiabatic temperature, compared to the *LamUnstbale* case, indicating that turbulence enhances thermodiffusive effects. Note that the high super-adiabatic values are also relevant for the formation of nitric oxides via the thermal pathway, which features an exponential dependence of their source term on temperature.

After the analysis of the mixture fraction distribution and scatter, it is of interest to assess the impact of mixture fraction fluctuations on the reaction rate. For this, Fig. 19 shows the progress variable source term conditionally averaged on progress variable and mixture fraction. In addition to the conditional averages $\langle Z|C_{H_2}\rangle$ and the unstretched flamelets, three iso-lines of $\dot{\omega}_C$ = 10, 100, and 1000 s^{-1} are shown to improve the visualization. $\dot{\omega}_C$ strongly non-linearly varies with C_{H_2} and Z in the two cases (note the logarithmic color scale), so the significantly higher fluctuations of mixture fraction in the *TurbUnstable* case also lead to significantly higher values of $\dot{\omega}_C$. In particular, the shift of the conditional mean towards higher mixture fraction values in the *TurbUnstable* case leads to a significant enhancement of reaction rates in the *TurbUnstable* case.

3.4.2. The Effects of Curvature on Differential Diffusion and Mixture Fraction Fluctuations

While mixture fraction was shown to adequately describe the effects of differential diffusion and being well suited to parametrize reaction rates and the local flame state, in the following, the relationship between mixture fraction and the topological parameters of the flame front, such as curvature and strain rate, which cause the fluctuations of mixture fraction, are discussed. Fig. 20 shows the distribution of stretch, strain rate, and curvature on the flame sheet. The turbulent cases reveal much broader distributions compared to the laminar flame while little differences are visible between the *TurbStable* and *TurbUnstable* cases. This is particularly pronounced for the strain rate. For curvature, similar minimum values are obtained for all flames, but significantly larger positive curvature values are seen in the turbulent flames. To highlight the link between mixture fraction fluctuations and curvature, Fig. 21 shows the conditional average of stretch, curvature, and strain rate with respect to progress variable C_{H_2} and mixture fraction Z for the *TurbUnstable* and *LamUnstable* cases. A good correlation of curvature and stretch with mixture fraction is observed. In addition, a good correspondence of the conditional mean of mixture fraction $\langle Z|C_{H_2}\rangle$ and the line of vanishing curvature is visible in Fig. 21, indicating that the fluctuations of mixture fraction are caused by positive or negative curvature values. This effect is similar in the laminar and turbulent flames; however, the existence of larger positive and negative values of curvature in the *TurbUnstable* case enhance this behavior. For the strain rate, a reduction of mixture fraction is seen for increasing values of strain rate. This trend is also visible in the laminar case but is less pronounced as there is overall less variation of the strain rate. However, the fluctuations of mixture fraction are mainly caused by the different values of curvature rather than the variations of the strain rate. To highlight this, an optimal estimator analysis concerning the fluctuations of mixture fraction is performed in Fig. 22 for the *TurbUnstable* case. The irreducible error is defined as

$$\epsilon_{\mathrm{irr},Z}^{\mathrm{norm}} = \frac{\langle\, (Z - \langle Z|\boldsymbol{\psi}\rangle)^2 \mid C_{H_2}\,\rangle}{Z_{\mathrm{eq}}^2}, \tag{24}$$

where Z_{eq} = 0.012 is the value in the fully mixed equilibrium region in the burned gas. The high irreducible errors associated with the parameter set $\psi = [C_{H_2}, K_S]$, which are indeed close to those obtained with $\psi = [C_{H_2}]$, demonstrate that the mixture fraction fluctuations depend on the variations of the strain rate only marginally. In contrast, irreducible errors are significantly reduced if curvature and progress variable are employed for the parametrization, indicating the strong link between mixture fraction and curvature. This is consistent with the optimal estimator analysis or the source term $\dot{\omega}_C$ as variations of $\dot{\omega}_C$ and mixture fraction are closely linked to each other. Thus, the strong curvature fluctuations due to turbulence and the subsequent response of the flame in terms of enhanced differential diffusion represent a synergistic coupling of turbulence and thermodiffusive instabilities.

3.4.3. The Effects of Strain Rate on Differential Diffusion: Scalar Gradients

While larger mixture fraction fluctuations in the *TurbUnstable* case compared to the *LamUnstable* case arise from

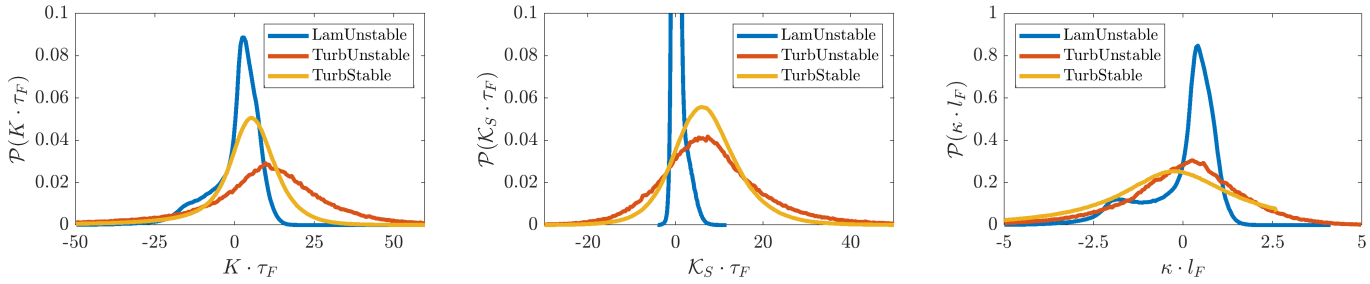

Figure 20: PDF of curvature, strain rate, and stretch on an iso-surface of $C_{\mathrm{H_2}} = 0.8$ for all three cases; statistics are collected at half of the flame height in the turbulent flames.

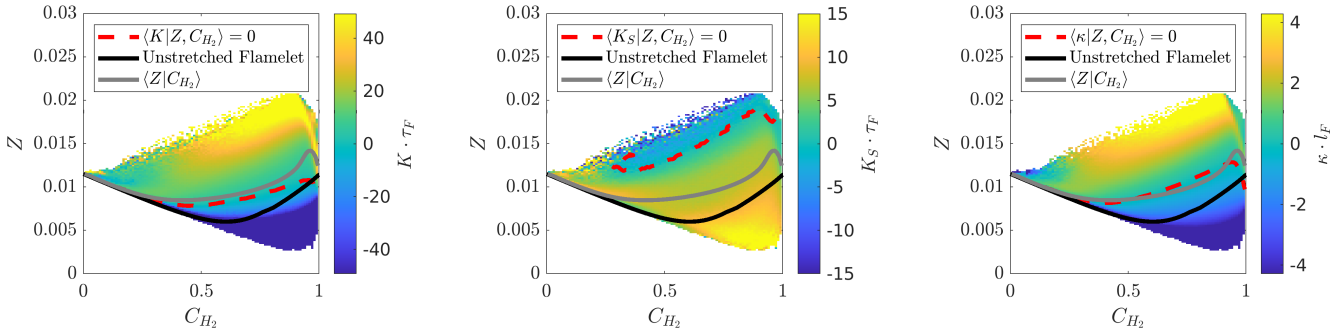

(a) *TurbUnstable* case

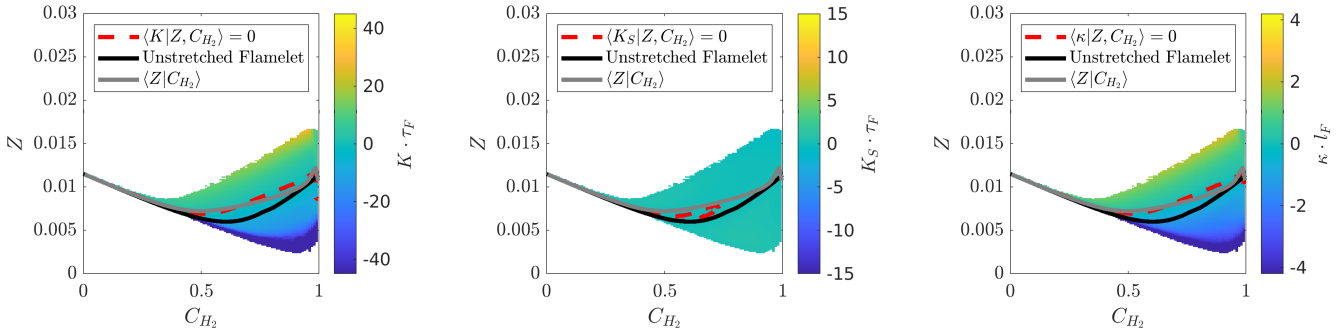

(b) *LamUnstable* case

Figure 21: Conditionally averaged stretch, strain rate, and curvature (left to right) with respect to $C_{\mathrm{H_2}}$ and Z. Additionally the line, where the conditional averages become zero (red dashed line), the conditional average $\langle Z|C_{\mathrm{H_2}}\rangle$, and the unstretched flamelet are displayed.

larger curvature values, the differences of the conditional means $\langle Z|C_{\mathrm{H_2}}\rangle$ in the *TurbUnstable* and *LamUnstable* cases, e.g., in Fig. 19, need to be discussed. In the following, this difference is shown to be linked to a significantly enhanced mean strain rate in the *TurbUnstable* flame compared to the *LamUnstable* case, which strongly affects the differential diffusion within the flame front and yields higher scalar gradients and reaction rates. For this, it is worth noting that the previously discussed insignificant reduction of irreducible errors of mixture fraction and the progress variable source term by strain rate in Figs. 16 and 22 only shows that the instantaneous flame response is insensitive to strain rate fluctuations, which has been similarly observed by Im et al. [65] in oscillating premixed counterflow flames at sufficienlty high frequencies. However, Im et al. [65] also showed that, in contrast to the fluctuations of strain rate, the mean strain rate still significantly affects the flame's consumption speed, which is similarly observed in this work and discussed in the following. In particular, an irreducible error analysis only assesses how well the fluctuations of a parameter correlate with the fluctuations of a quantity of interest, so irreducible errors remain unaffected by a shift of the mean values, e.g. by a larger mean strain rate in the *TurbUnstable* case compared to the *LamUnstbale* case. In the following, the effects of the mean strain rate on scalar gradients and the local reaction rates are discussed and to disentangle the effects of curvature and strain rate in the *TurbUnstable* and *LamUnstable* flames, a comparison to laminar premixed counterflow flames is performed.

Fig. 23 shows the gradient of progress variable $|\nabla C_{\mathrm{H_2}}|$ conditionally averaged with respect to progress variable for all cases. For comparison, the values are normalized with the maximum gradient $\max(|\nabla C_{\mathrm{H_2}}|)$ obtained in the corresponding unstretched laminar flamelets (two flamelets are computed; one with the diffusivity model of case *TurbUnstable*, which is used for the normalization of the *TurbUnstable* and the *LamUnstable* case and

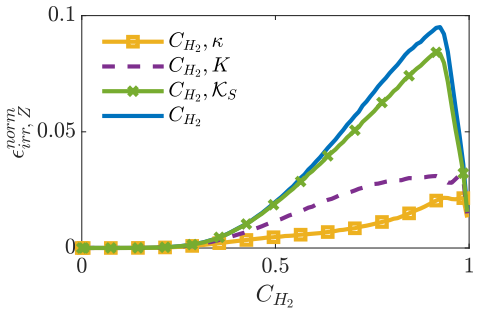

Figure 22: *TurbUnstable* case: Irreducible errors of mixture fraction Z if parametrized by different sets of parameters.

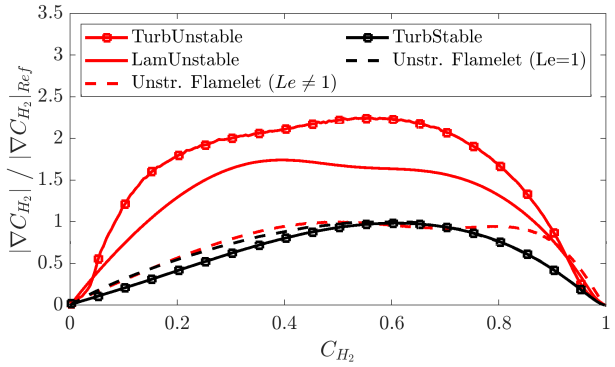

Figure 23: Conditional average of the progress variable gradient $|\nabla C_{\mathrm{H_2}}|$ with respect to $C_{\mathrm{H_2}}$ for all three cases and the two flamelets, which have been computed with the diffusivity models of the *TurbUnstable* and *TurbStable* case and are labeled by $Le \neq 1$ and $Le = 1$, respectively. The gradients are normalized by $|\nabla C_{\mathrm{H_2}}|_{\mathrm{Ref}}$, which is the maximum gradient $\max(|\nabla C_{\mathrm{H_2}}|)$ of the corresponding unstretched laminar flamelet.

one with the diffusivity model of case *TurbStable*, which is used to normalize the *TurbStable* case). In the *TurbUnstable* and *LamUnstable* cases, an increase of $|\nabla C_{\mathrm{H_2}}|$ and, hence, a reduction of flame thickness is observed compared to the unstretched flamelet; however, in the turbulent *TurbUnstable* flame, this effect is much more pronounced. In contrast, for the *TurbStable* case, the mean progress variable gradients are very similar to an unstretched flamelet, while a small reduction of gradients and, hence, flame thickening is observed for small values of the progress variable.

To disentangle the effect of curvature and strain rate on the progress variable gradient $|\nabla C_{\mathrm{H_2}}|$, Fig. 24 shows the conditional mean of the gradient $|\nabla C_{\mathrm{H_2}}|$ on curvature κ for an iso-surface of progress variable at $C_{\mathrm{H_2}} = 0.8$ for the three cases. As expected, large positive and negative values of curvature lead to a reduction of $|\nabla C_{\mathrm{H_2}}|$ as highly curved flame segments typically lead to a thickening of the flame. While this reduction is symmetric for the *TurbStable* case, a skewed distribution is seen for the *TurbUnstable* and *LamUnstable* case. This relates to the thermodiffusive instability mechanism as positive curvature values represent flame segments with higher mixture fractions and, hence, higher reaction rates, which lead to a steepening of gradients. To highlight this, Fig. 25 shows the conditional average of $\dot{\omega}_{\mathrm{C}}$ with respect to κ, indicating a strong increase of $\dot{\omega}_{\mathrm{C}}$ towards positive curvature values. As this effect counteracts the flame thickening with increasing curvature values, an asymmetric profile of $|\nabla C_{\mathrm{H_2}}|$ with respect to κ is obtained in the *TurbUnstable* and *LamUnstable* case. However, in the *TurbStable* case, no variation of $\dot{\omega}_{\mathrm{C}}$ with κ is seen, as $\dot{\omega}_{\mathrm{C}}$ was shown to closely follow the flamelet solution in Fig. 15b, yielding a symmetric profile of $|\nabla C_{\mathrm{H_2}}|$ with respect to κ. Further details on the reaction rates are discussed at the end of this subsection.

For all flames, the value of $|\nabla C_{\mathrm{H_2}}|$ at $\kappa = 0$, which represents a locally flat flame, is significantly different from the value of the unstretched laminar flamelet that is used for normalization. This is caused by the mean positive strain rate. In the turbulent flames, the mean positive strain rate was shown to be determined by the smallest turbulent eddies, yielding $\langle K_{\mathrm{S}} \rangle_{\mathrm{S}} \tau_\eta \approx 0.28$ or $\langle K_{\mathrm{S}} \rangle_{\mathrm{S}} \tau_F \approx 6.5$, respectively, and also for the *LamUnstable* case, a positive mean strain rate of $\langle K_{\mathrm{S}} \rangle_{\mathrm{S}} \tau_F \approx 0.4$ is obtained. $\langle K_{\mathrm{S}} \rangle_{\mathrm{S}}$ is significantly smaller in the *LamUnstable* case compared to the turbulent flames since the effect of turbulence is missing and the strain rate is only determined by the flame intrinsic instability mechanism. To highlight the effect of the mean strain rate on the progress variable gradient, the value of $|\nabla C_{\mathrm{H_2}}|$ of laminar premixed counterflow flames that are exposed to the same strain rate as the *TurbUnstable*, *TurbStable*, and *LamUnstable* flames are depicted in Fig. 24 (green dot) and good agreement with the value $|\nabla C_{\mathrm{H_2}}|$ at $\kappa = 0$ is seen. For reference, the value of $\dot{\omega}_{\mathrm{C}}$ of the same counterflow flame is also depicted in Fig. 25, indicating good agreement[3]. In the counterflow configuration, unburned and burned gas are injected against each other from two opposed nozzles and computations have been performed with the FlameMaster code [47]. The same diffusion models and reaction mechanism as for the turbulent flames have been applied (constant Lewis numbers and the inclusion of the Soret effect in the *TurbUnstable* case and unity Lewis numbers and no Soret effect in the *TurbStable* case). To compare the strain rate within the turbulent and counterflow flames, Fig. 26 shows a comparison of the conditional average of the normal and tangential component of the strain rate tensor, a_{N} and K_{S}, where the former is defined as

$$a_{\mathrm{N}} = \boldsymbol{n} \cdot \nabla \boldsymbol{u} \cdot \boldsymbol{n}, \tag{25}$$

and the dilatation term $\nabla \cdot \boldsymbol{u}$ in the *TurbUnstable* case and the corresponding values of a counterflow flame. The conditions of the counterflow flame are chosen such that the same tangential strain rate is obtained within the counterflow and turbulent flame.

A positive constant value of the tangential strain rate, which corresponds to $\langle K_{\mathrm{S}} \rangle_{\mathrm{S}} \tau_\eta \approx 0.28$ if normalized by τ_η instead of τ_{F}, is observed throughout the flame and generally, good agreement of the local tangential and normal strain rates among the laminar counterflow flame and the *TurbUnstable* case is observed. Further, the evolution of these terms is consistent with the findings of Chakraborty et al. [55], who found that for low

[3]Note that small discrepancies are still seen since curvature fluctuations and strain rate, while being the cause of differential diffusion, are not as well suited for the parametrization of the source term as mixture fraction, as pointed out by the irreducible error analysis.

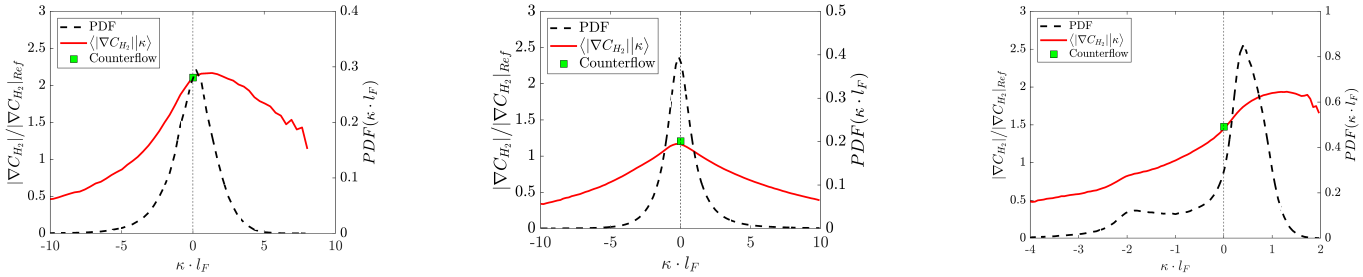

(a) *TurbUnstable* case (b) *TurbStable* case (c) *LamUnstable* case

Figure 24: Dependency of $|\nabla C_{H_2}|$ on curvature for the *TurbUnstable*, *TurbStable*, and *LamUnstable* case (left to right) on an iso-surface of $C_{H_2} = 0.8$. The gradients are normalized by $|\nabla C_{H_2}|_{Ref}$, which is the gradient $|\nabla C_{H_2}|$ in an unstretched laminar flamelet at $C_{H_2} = 0.8$. Note that two different flamelets with the two different diffusivity models are used; one to normalize the cases *TurbUnstable* and *LamUnstable* and one for the *TurbStable* case. The green dot represents $|\nabla C_{H_2}|$ in the selected counterflow flame for each turbulent flame.

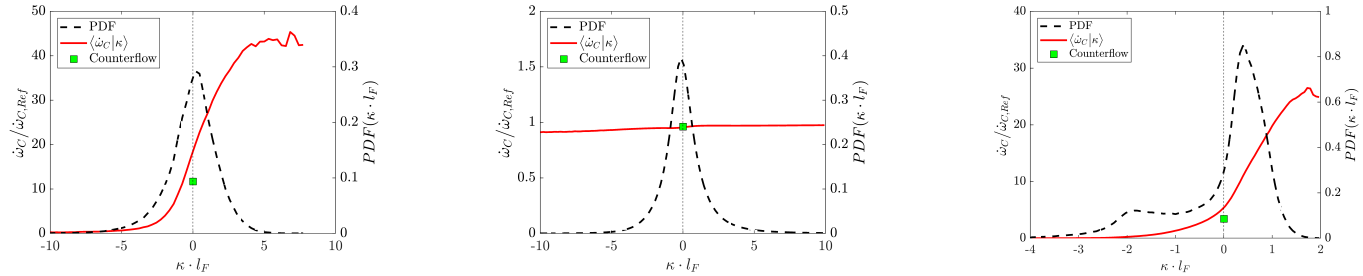

(a) *TurbUnstable* case (b) *TurbStable* case (c) *LamUnstable* case

Figure 25: Dependency of $\dot{\omega}_C$ on curvature for the *TurbUnstable*, *TurbStable*, and *LamUnstable* case (left to right) on an iso-surface of $C_{H_2} = 0.8$. $\dot{\omega}_C$ is normalized by $\dot{\omega}_{C,Ref}$, which is the value of $\dot{\omega}_C$ in an unstretched laminar flamelet at $C_{H_2} = 0.8$. Note that two different flamelets with the two different diffusivity models are used; one to normalize the cases *TurbUnstable* and *LamUnstable* and one for the *TurbStable* case. The green dot represents $\dot{\omega}_C$ in the selected counterflow flame for each turbulent flame.

Karlovitz number flames, in which the heat release or dilatation term, respectively, dominates the normal strain rate, as shown in Fig. 26 for the *TurbUnstable* case, the flame tends to align with the most compressive principal strain rate for low progress variable values yielding a negative normal strain rate and with the most extensive principal strain rate for intermediate values of progress variable due to the heat release leading to positive values of the normal strain rate. Reasonable agreement of the tangential and normal strain rate and the dilation term with the premixed counterflow flames is also obtained for the *TurbStable* and *LamUnstable* cases as shown in Figs. A8 and A9 in the supplementary material.

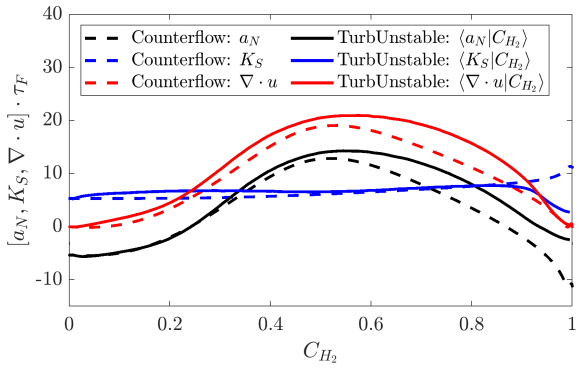

Figure 26: Comparison of normal and tangential strain rate and dilatation term in a selected counterflow flame (dashed line) with the conditional averages obtained in the *TurbUnstable* case (solid line).

3.4.4. The Effects of Strain Rate on Differential Diffusion: Mixture Fraction Variations

In the previous section, the analysis of the local flame state by means of curvature and strain rate showed that local progress variable gradients and reaction rates are strongly affected by curvature and the mean positive strain rate. In this section, the effects of the mean strain rate on mixture fraction and, in particular, the difference of the conditional mean mixture fraction $\langle Z|C_{H_2} \rangle$ compared to the unstretched flamelet solution in the *TurbUnstable* and *LamUnstable* cases are discussed.

To highlight the effect of strain rate on the differential diffusion of hydrogen and the local flame state for the *TurbUnstable* case, Fig. 27 shows the evolution of the normalized mass fractions of water Y_{H_2O} and hydrogen Y_{H_2}, mixture fraction Z, and the progress variable source term $\dot{\omega}_C$ in space for the selected counterflow flame in comparison to an unstretched planar flamelet; both are computed with the diffusion model employed in the *TurbUnstable* case. It is evident that the counterflow flame features a significantly thinner flame with higher gradients and that the mean positive strain rate sensitively affects the reaction rates, diffusive fluxes, and, in particular, the differential diffusion of hydrogen within the flame. During the consumption of hydrogen, the counterflow flame features higher mixture fraction values, which corresponds to a burning behavior at a higher local equivalence ratio, leading to sig-

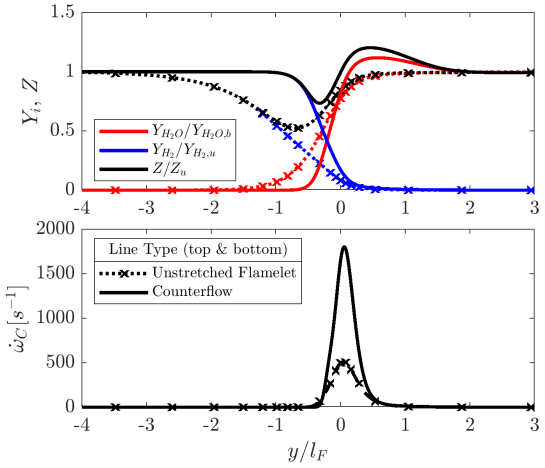

Figure 27: Comparison of Y_{H_2O}, Y_{H_2}, Z, and $\dot{\omega}_C$ in a selected counterflow flame (solid line) and an unstretched flamelet (dashed line) using the diffusivity model of the *TurbUnstable* case. For both cases, the spatial coordinate is normalized by the thermal flame thickness l_F of the unstretched laminar flame. The consumption speeds of the counterflow and unstretched flames are s_c = 0.49 m/s and s_c = 0.17 m/s, respectively.

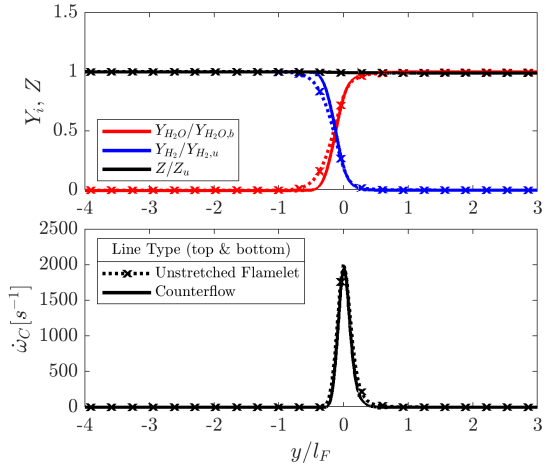

Figure 28: Comparison of Y_{H_2O}, Y_{H_2}, Z, and $\dot{\omega}_C$ in a selected counterflow flame (solid line) and an unstretched flamelet (dashed line) using the diffusivity model of the *TurbStable* case. For both cases, the spatial coordinate is normalized by the thermal flame thickness l_F of the unstretched laminar flame. The consumption speeds of the counterflow and unstretched flames are s_c = 0.32 m/s and s_c = 0.34 m/s, respectively.

nificantly higher reaction rates and super-equilibrium values of the combustion products, such as water and temperature, in the post-flame region. This is also reflected by a significantly increased consumption speed of the counterflow flame[4], which is s_c = 0.49 m/s compared to s_c = 0.17 m/s in the unstretched flamelet. For the diffusivity model of case *TurbStable* (unity Lewis numbers and no Soret effect), the same comparison of a counterflow flame, which is selected such that its tangential strain rate matches the value of the *TurbStable* case, and an unstretched flamelet is shown in Fig. 28. A significantly smaller reduction of flame thickness is observed among the counterflow and unstretched flame compared to the flames that include the effects of differential diffusion in Fig. 27. By construction, a constant mixture fraction is obtained for the counterflow and unstretched flame in Fig. 28, as differential diffusion is suppressed, and the effect of strain rate is found to have almost no effect on the progress variable source term. Hence, the strong reduction of flame thickness in Fig. 27, which includes the effects of differential diffusion, is not only caused by the compression of the flame due to the flow field, but is also strongly linked to the enhancement of reaction rates in this case. In other words, the enhancement of gradients due to the positive strain rate leads to higher reaction rates, which further steepens the flame, yielding eventually a significantly thinner flame with significantly higher reaction rates. To highlight the strong sensitivity of the reaction rates and scalar gradients to strain rate if the effects of differential diffusion are considered, the variations of $\dot{\omega}_C$ and $|\nabla C_{H_2}|$ with different strain rates in counterflow flamelets are shown for the two diffusivity models in Fig. A11 in the supplementary material. These findings are consistent with Fig. 24 for the turbulent flames, where the increase of gradients and reaction rates is much more pronounced in the *TurbUnstable* case than in the *TurbStable* case.

A comparison of the conditional mean $\langle Z|C\rangle$ of the *TurbUnstable* and *LamUnstable* cases with the profile of mixture fraction in progress variable space for the selected counterflow flames is shown in Fig. 29. Further, the profiles of the unstretched flamelet and an additional counterflow flamelet featuring a tangential strain rate that is significantly larger than the *TurbUnstable* case are shown to highlight the effect of strain rate on mixture fraction. It is evident that higher strain rates lead to an enhancement of mixture fraction during the combustion process. Further, good agreement between the conditional mean $\langle Z|C\rangle$ of the *TurbUnstable* and *LamUnstable* cases and the selected counterflow flamelets is observed, indicating that the shift towards higher mixture fractions is caused by the mean strain due to turbulence. Thus, the super-equilibrium values of Y_{H_2O} in Fig. 5 that are seen in the post flame region around the flame (the flame is shielded by red colors while a yellow color is seen in the coflow) can be linked to the mean positive strain rates, which lead to an overshoot similar to that observed in a counterflow flame.

3.5. *Effects of the Local Flame State on the Stretch Factor*

In this section, the variations of the heat release and flame thickness in the *TurbUnstable* case are linked to the strongly enhanced stretch factor $I_0 \approx 4$ and contrasted with the *TurbStable* and *LamUnstable* case, where values of $I_0 \approx 1$ and $I_0 = 2.6$ are observed, respectively. Generally, a non-unity value of I_0 can be obtained if the local fuel consumption rate deviates from the values in an unstretched flamelet solution or if variations of the local flame thickness occur as I_0 is computed by the integral of reaction rates across the entire flame, cf. Eq. 7 and Attili et al. [52]. Thus, the unity value of I_0 for the *TurbStable* case and the previous analyses of the reaction rates and flame thickness indicate a local burning that is close to a laminar unstretched

[4] s_c is computed according to Eq. 7

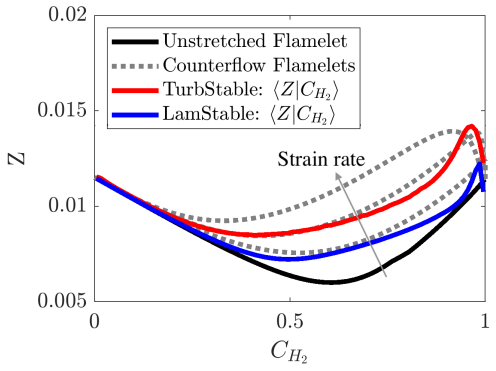

Figure 29: Comparison of the conditional mean mixture fraction with respect to progress variable in the *TurbUnstable* case (red line) and *LamUnstable* case (blue line), three selected counterflow flames at different strain rates, $K_S \cdot \tau_F \approx$ 0.4, 6.5, 30, (grey dotted lines) and the unstretched flamelet (black line). The arrow indicates the direction of increasing strain rate.

flamelet. In particular, Figs. 25 and 24 suggest that there is a small variability of $|\nabla C_{\mathrm{H_2}}|$, which is a measure of flame thickness, and reaction rates with respect to the unstretched flamelet, but both effects compensate each other to yield $I_0 \approx 1$.

In the thermodiffusively unstable cases *TurbUnstable* and *LamUnstable*, super-unity values of I_0 are obtained due to the significant increase of reaction rates compared to the unstretched flamelet. While the flame fronts become thinner, as indicated by the increase of gradients $|\nabla C_{\mathrm{H_2}}|$ in Fig. 24, this effect is overcompensated by the increase of reaction rates. In particular, Fig. 25 shows up to 40 times higher reaction rates in the *TurbUnstable* case compared to an unstretched flamelet, while it is worth stressing that almost no effect on the flame reactivity is seen in the *TurbStable* case. As reaction rates are significantly larger in the *TurbStable* compared to the *LamUnstable* case due to the larger fluctuations of curvature and the mean positive strain rate and only a maximum increase of gradients by a factor of two is seen in the *TurbStable* case, a larger overcompensation occurs in the turbulent flame, yielding a higher value of I_0.

4. Conclusion

Large-scale Direct Numerical Simulations of three-dimensional premixed lean hydrogen/air flames have been performed in a slot burner configuration to study the interactions of turbulence and thermodiffusive instabilities. Two jet flames at the same jet Reynolds number of $Re = 11,000$ and Karlovitz number of $Ka \approx 15$ with different diffusivity models were computed. Realistic diffusivities were employed in one case while in the other case, the diffusivities of all species were set to the thermal diffusivity to suppress thermodiffusive instabilities. The thermodiffusively unstable flame clearly shows the typical features of thermodiffusive instabilities such as super-adiabatic temperatures, local extinction, and a significant enhancement of the turbulent flame speed resulting in a significantly shorter flame due to more intense burning. For the analysis, the turbulent flame speed is split into contributions arising from the wrinkling of the flame surface area and the effects due to variations of the heat release.

As the generation and destruction of flame surface area is determined by the surface-averaged stretch rate, an analysis of the different components of stretch, such as the tangential strain rate and the product of curvature and the flame displacement speed, was performed. Most noteworthy, the generation of surface area due to strain rate is found to be similar in both flames and, in particular, to be governed by the smallest scales of turbulence rather than flame intrinsic processes. For the curvature term, the three following conclusions were drawn: i) the destruction of flame surface area in the cusp regions due to flame propagation was found to be similar in both turbulent flames, ii) the thermodiffusively unstable flame features a strong surface area generation in flame segments that are convexly curved towards the unburned gas, leading to the formation of tongue-like structures that penetrate into the unburned gas and do not exist in the stable turbulent flame, and iii) the flame surface area generation and destruction by the curvature term and, in particular, the formation of the tongue-like structures are significantly enhanced in the thermodiffusively unstable turbulent flame compared to a thermodiffusively unstable laminar flame as higher curvature values are obtained in the turbulent environment, indicating a synergistic interaction between instabilities and turbulence.

Thermodiffusive instabilities are found to lead to significant fluctuations of the local equivalence ratio and, hence, feature strong variations of the local reactivity. These fluctuations are closely linked to the local curvature of the flame front and a comparison with a laminar thermodiffusively unstable flame shows that these effects are significantly enhanced in a turbulent flame, as significantly higher curvature fluctuations prevail in the turbulent flow. Further, the mean positive strain due to turbulence was shown to steepen scalar gradients, which significantly affects the differential diffusion of hydrogen, leading to an enhancement of the mean mixture fraction and, hence, higher mean reaction rates within the turbulent flame. Both effects represent synergistic interactions of turbulence and thermodiffusive instabilities as higher curvature values and the mean strain rate in the turbulent flow amplify the effects of differential diffusion. This is also reflected in a significantly higher stretch factor I_0 in the turbulent flame of $I_0 = 4$, while a value of $I_0 = 2.6$ is obtained in the laminar thermodiffusively unstable flame.

These findings suggest that thermodiffusive instabilities are sustained in turbulent flows and even show synergistic interactions with turbulence, which needs to be accounted for in turbulent combustion models.

Acknowledgment

Generous support of the Deutsche Forschungsgemeinschaft (DFG) under grant number PI 368/9-1 is gratefully acknowledged. Computational resources have been provided by the Gauss Centre for Supercomputing e.V. on the GCS Supercomputer SuperMuc at Leibniz Supercomputing Centre in Munich.

References

[1] J. Perner, D. Bothe, Report for the World Energy Council German by Frontier Economics Ltd. (2018).

[2] A. Sartbaeva, V.L. Kuznetsov, S.A. Wells, P.P. Edwards, Hydrogen nexus in a sustainable energy future, Energ. Environ. Sci. 1 (2008) 79–85.

[3] S. Verhelst, T. Wallner, Hydrogen-fueled internal combustion engines, Prog. Energ. Combust. 35 (2009) 490–527.

[4] L. Berger, K. Kleinheinz, A. Attili, H. Pitsch, Characteristic patterns of thermodiffusively unstable premixed lean hydrogen flames, Proc. Comb. Inst. 37 (2019) 1879–1886.

[5] S. Kadowaki, T. Hasegawa, Numerical simulation of dynamics of premixed flames: flame instability and vortex–flame interaction, Prog. Energ. Combust. 31 (2005) 193–241.

[6] J. Yuan, Y. Ju, C. K. Law, On flame-front instability at elevated pressures, Proc. Comb. Inst. 31 (2007) 1267–1274.

[7] C. Altantzis, C. E. Frouzakis, A. G. Tomboulides, S. G. Kerkemeier, K. Boulouchos, Detailed numerical simulations of intrinsically unstable two-dimensional planar lean premixed hydrogen/air flames, Proc. Comb. Inst. 33 (2011) 1261–1268.

[8] C.E. Frouzakis, N. Fogla, A.G. Tomboulides, C. Altantzis, M. Matalon, Numerical study of unstable hydrogen/air flames: Shape and propagation speed, Proc. Combust. Inst. 35 (2015) 1087–1095.

[9] J.F. Yu, R. Yu, X.S. Bai, M.B. Sun, J.G. Tan, Nonlinear evolution of 2D cellular lean hydrogen/air premixed flames with varying initial perturbations in the elevated pressure environment, Int. J. Hydrogen Energ. 42 (2017) 3790–3803.

[10] D. Fernández-Galisteo, V.N. Kurdyumov, P.D. Ronney, Analysis of premixed flame propagation between two closely-spaced parallel plates, Combust. Flame 190 (2018) 133–145.

[11] L. Berger, A. Attili, H. Pitsch, Intrinsic Instabilities in Premixed Hydrogen Flames: Parametric Variation of Pressure, Equivalence Ratio, and Temperature. Part 1 - Dispersion Relations in the Linear Regime, Combust. Flame (2021) accepted.

[12] L. Berger, A. Attili, H. Pitsch, Intrinsic Instabilities in Premixed Hydrogen Flames: Parametric Variation of Pressure, Equivalence Ratio, and Temperature. Part 2 - Non-Linear Regime and Flame Speed Enhancement, Combust. Flame (2021) accepted.

[13] H. Boughanem, A. Trouvé, The domain of influence of flame instabilities in turbulent premixed combustion, Proc. Comb. Inst. 27 (1998) 971–978.

[14] V. Bychkov, Importance of the Darrieus-Landau instability for strongly corrugated turbulent flames, Phys. Rev. E 68 (2003).

[15] S. Chaudhuri, V. Akkerman, C.K. Law, Spectral formulation of turbulent flame speed with consideration of hydrodynamic instability, Phys. Rev. E 84 (2011).

[16] J.H. Chen, H.G. Im, Stretch effects on the burning velocity of turbulent premixed hydrogen/air flames, Proc. Comb. Inst. 28 (2000) 211–218.

[17] H.G. Im, J.H. Chen, Preferential Diffusion Effects on the Burning Rate of Interacting Turbulent Premixed Hydrogen-Air Flames, Combust. Flame 131 (2002) 246–258.

[18] E.R. Hawkes, J.H. Chen, Direct numerical simulation of hydrogen-enriched lean premixed methane–air flames, Combust. Flame 138 (2004) 242–258.

[19] N. Chakraborty, E.R. Hawkes, J.H. Chen, R.S. Cant, The effects of strain rate and curvature on surface density function transport in turbulent premixed methane–air and hydrogen–air flames: A comparative study, Combust. Flame 154 (2008) 259–280.

[20] A.J. Aspden, M.S. Day, J.B. Bell, Characterization of low Lewis number flames, Proc. Comb. Inst. 33 (2011) 1463–1471.

[21] A.J. Aspden, M.S. Day, J.B. Bell, Lewis number effects in distributed flames, Proc. Comb. Inst. 33 (2011).

[22] A.J. Aspden, M.S. Day, J.B. Bell, Turbulence-flame interactions in lean premixed hydrogen: transition to the distributed burning regime, J. Fluid Mech. 680 (2011) 287–320.

[23] A.J. Aspden, M.S. Day, J.B. Bell, Turbulence-chemistry interaction in lean premixed hydrogen combustion, Proc. Comb. Inst. 35 (2015) 1321–1329.

[24] E.R. Hawkes, O. Chatakonda, H. Kolla, A.R. Kerstein, J.H. Chen, A petascale direct numerical simulation study of the modelling of flame wrinkling for large-eddy simulations in intense turbulence, Combust. Flame 159 (2012) 2690–2703.

[25] J.F. MacArt, T. Grenga , M.E. Mueller, Effects of combustion heat release on velocity and scalar statistics in turbulent premixed jet flames at low and high Karlovitz numbers, Combust. Flame 191 (2018) 468–485.

[26] M.S. Wu, S. Kwon, J. F. Driscoll, G.M. Faeth, Preferential Diffusion Effects on the Surface Structure of Turbulent Premixed Hydrogen/Air Flames, Combust. Sci. Technol. 78 (1991) 69–96.

[27] P. Ahmed, B. Thorne, M. Lawes, S. Hochgreb, G.V. Nivarti, R.S. Cant, Three dimensional measurements of surface areas and burning velocities of turbulent spherical flames, Combust. Flame 233 (2021).

[28] G. Rocco, F. Battista, F. Picano, G. Troiani, C.M. Casciola, Curvature Effects in Turbulent Premixed Flames of H2/Air: a DNS Study with Reduced Chemistry, Flow Turbul. Combust. 94 (2015) 359–379.

[29] Z. Zhou, F.E. Hernandez-Perez, Y. Shoshin, J.A. van Oijen, L.P.H. de Goey, Combust. Theor. Model. 21 (2017) 879–896.

[30] J. Schlup, G. Blanquart, Validation of a mixture-averaged thermal diffusion model for premixed lean hydrogen flames, Combust. Theor. Model. 22 (2018) 264–290.

[31] R. Sankaran, E.R. Hawkes, J.H. Chen, T. Lu, C.K. Law, Structure of a spatially developing turbulent lean methane–air Bunsen flame, Proc. Comb. Inst. 31 (2007) 1291–1298.

[32] S. Luca, A.N. Al-Khateeb, A. Attili, F. Bisetti, Comprehensive validation of skeletal mechanism for turbulent premixed methane-air flame simulations, J. Propul. Power 34 (2018) 153–160.

[33] C. Patano, S. Sarkar, F.A. Williams, Mixing of a conserved scalar in a turbulent reacting shear layer, J. Fluid Mech. 428 (2003) 291–328.

[34] A.G. Tomboulides, J.C.Y. Lee, S.A. Orszag, Numerical Simulation of Low Mach Number Reactive Flows, J. Scientif. Comput. 12 (1997) 139–167.

[35] M.P. Burke, M. Chaos, Y. Ju, F.L. Dryer, S.J. Klippenstein, Comprehensive H_2/O_2 kinetic model for high-pressure combustion, Int. J. Chem. Kinet. 44 (2012) 444–474.

[36] C.R. Wilke, A Viscosity Equation for Gas Mixtures, J. Chem. Phys. 18 (1950) 517–519.

[37] R.B. Bird, W.E. Stewart, E.N. Lightfoot, Transport Phenomena, John Wiley & Sons, Inc., 2007.

[38] A. Eucken, Über das Wärmeleitvermögen,die spezifische Wärme und die innere Reibung der Gase, Physik. Z. 14 (1913).

[39] S. Mathur, P. Tondon, S. Saxena, Thermal conductivity of binary, ternary and quaternary mixtures of rare gases, Mol. Phys. 12 (1967) 569–579.

[40] J. Schlup, G. Blanquart, A reduced thermal diffusion model for H and H_2, Combust. Flame 191 (2018) 1–8.

[41] A. Attili, F. Bisetti, M.E. Mueller, H. Pitsch, Effects of non-unity Lewis number of gas-phase species in turbulent nonpremixed sooting flames, Combust. Flame 166 (2016) 192–202.

[42] O. Desjardins, G. Blanquart, G. Balarac, H. Pitsch, J. Comput. Phys. 227 (2008) 7125–7159.

[43] R.D. Falgout, U.M. Yang, hypre: A library of high performance preconditioners, in: Computational Science—ICCS 2002, Springer, 2002, pp. 632–641.

[44] G.S. Jiang, C.W. Shu, Efficient Implementation of Weighted ENO Schemes, J. Comput. Phys. 126 (1996) 202–228.

[45] G. Strang, On the Construction and Comparison of Difference Schemes, SIAM J. Numer. Anal. 5 (1968) 506–517.

[46] A.C. Hindmarsh, P.N. Brown, N. Peter, K.E. Grant, S.L. Lee, R. Serban, D.E. Shumaker, C.S. Woodward, SUNDIALS: Suite of nonlinear and differential/algebraic equation solvers, ACM T. Math. Software 31 (2005) 363–396.

[47] H. Pitsch, A C++ program package for 0D combustion and 1D laminar flames, 1998.

[48] R.W. Bilger, S.H. Starner, R.J. Kee, On reduced mechanisms for methane-air combustion in nonpremixed flames, Combust. Flame 80 (1990) 135–149.

[49] J.D. Regele, E. Knudsen, H. Pitsch, G. Blanquart, Combust. Flame 160 (2013) 240–250.

[50] T.M. Wabel, R.S. Barlow, A.M. Steinberg, Reaction zone stratification in piloted highly-turbulent fuel-lean premixed jets, Combust. Flame 208 (2019) 327–329.

[51] A. Attili, K. Kleinheinz, D. Denker, L. Berger, F. Bisetti, H. Pitsch, Mixing and entrainment of burned products in high Karlovitz number premixed jet flames, Proceedings of the European Combustion Meeting (2019).

[52] A. Attili, S. Stefano, D. Denker, F. Bisetti, H. Pitsch, Turbulent flame speed and reaction layer thickening in premixed jet flames at constant Karlovitz and increasing Reynolds numbers, Proc. Comb. Inst. 38 (2020) 2939–2947.
[53] L. Vervisch, E. Bidaux, K.N.C. Bray, W. Kollmann, Surface density function in premixed turbulent combustion modeling, similarities between probability density function and flame surface approaches, Phys. Fluids 7 (1995) 2496–2503.
[54] T. Poinsot, D. Veynante, Theoretical and numerical combustion, Edwards, 2005.
[55] N. Chakraborty, M. Klein, N. Swaminathan, Effects of Lewis number on the reactive scalar gradient alignment with local strain rate in turbulent premixed flames, Proc. Comb. Inst. 32 (2009) 1409–1417.
[56] C.J. Rutland, A. Trouvé, Direct Simulations of Premixed Turbulent Flames with Nonunity Lewis Numbers, Combust. Flame 94 (1993) 41–57.
[57] D.C. Haworth, T.J. Poinsot, Numerical simulations of Lewis number effects in turbulent premixed flames, J. Fluid Mech. 244 (1992) 405–436.
[58] P.K. Yeung, S.S. Grimaji, S.B. Pope, Straining and Scalar Dissipation on Material Surfaces in Turbulence: Implications for Flamelets, Combust. Flame 79 (1990) 340–365.
[59] S. Luca, A. Attili, E.L. Schiavo, F. Creta, F. Bisetti, On the statistics of flame stretch in turbulent premixed jet flames in the thin reaction zone regime at varying Reynolds number, Proc. Comb. Inst. 37 (2019) 2451–2459.
[60] N. Peters, Turbulent Combustion, Cambridge University Press, 2000.
[61] A. Moreau, O. Teytaud, J. P. Bertoglio, Optimal estimation for large-eddy simulation of turbulence and application to the analysis of subgrid models, Phys. Fluids 18 (2006).
[62] L. Berger, K. Kleinheinz, A. Attili, F. Bisetti, H. Pitsch, M.E. Mueller, Combust. Theor. Model. 22 (2018) 480–504.
[63] A.Y. Klimenko, A.G. Class, Propagation of non-stationary curved and stretched premixed flames with multi-step reaction mechanisms, Combust. Sci. Technol. 174 (2002) 165–207.
[64] M. Day, S. Tachibana, J. Bell, M. Lijewski, V. Beckner, R.K. Cheng, A combined computational and experimental characterization of lean premixed turbulent low swirl laboratory flames II. Hydrogen flames, Combust. Flame 162 (2015) 2148–2165.
[65] H.G. Im, J.H. Chen, Effects of flow transients on the burning velocity of laminar hydrogen/air premixed flames, Proc. Comb. Inst. 28 (2000) 1833–1840.